

Submitted to JAS on May 30, 2001
Revision I January 16, 2002
Revision II May 23, 2002
Accepted for publication in JAS July 1, 2002
To be published late 2002 or early 2003

Mechanism for the Generation of Secondary Waves in Wave Breaking Regions

Sharon L. Vadas,^a

David C. Fritts,

M. Joan Alexander

NorthWest Research Associates, Inc., Colorado Research Associates Division

3380 Mitchell Lane, Boulder, CO 80301

^aElectronic mail: vasha@colorado-research.com

We propose that the body force which accompanies wave breaking is potentially an important linear mechanism for generating secondary waves that propagate into the mesosphere and lower thermosphere. While the focus of our paper is on 3D forcings, we show that this generating mechanism can explain some of the mean wind and secondary wave features generated from wave breaking in a 2D nonlinear model study. Deep, 3D body forces, which generate secondary waves very efficiently, create high-frequency waves with large vertical wavelengths that possess large momentum fluxes. The efficiency of this forcing is independent of latitude. However, the spatial and temporal variability/intermittency of a body force is important in determining the properties and associated momentum fluxes of the secondary waves. High spatial and temporal variability accompanying a wave breaking process leads to large secondary wave momentum fluxes. If a body force varies slowly with time, negligible secondary wave fluxes result. Spatial variability is important because distributing “averaged” body forces over larger regions horizontally (as is often necessary in GCM models) results in waves with smaller frequencies, larger horizontal wavelengths, and smaller associated momentum fluxes than would otherwise result. Because some of the secondary waves emitted from localized body force regions have large vertical wavelengths and large intrinsic phase speeds, we anticipate that secondary wave radiation from wave breaking in the mesosphere may play a significant role in the momentum budget well into the thermosphere.

1. Introduction

Numerous model studies have shown that wave breaking generates secondary waves (Bacmeister and Schoeberl, 1989; Franke, 1996; Holton and Alexander, 1999a; Franke and Robinson, 1999; Satomura and Sato, 1999; Walterscheid and Schubert, 1990; Huang et al. 1992; Andreassen et al., 1994; Prusa et al., 1996; Andreassen et al., 1998; Fritts et al., 1998; LeLong and Dunkerton, 1998; Liu et al., 1999). High-resolution 3D studies where wave breaking occurs via convective instability show that the cascade to smaller scales (i.e., the transition to turbulence) occurs via nonlinear vortex interactions (Fritts et al., 1994; Andreassen et al., 1998; Fritts et al., 1998). In 2D studies, the wave breakdown takes longer to occur, and follows differing instability and vortex dynamic paths for late times as compared to 3D wave breaking (Andreassen et al., 1994; Fritts et al., 1994). Thus, 2D simulations do not capture many of the essential features that occur during wave breaking. During both 2D and 3D wave breaking, however, momentum and heat are deposited.

As is well known (Andrews et al., 1987), the vertical divergence of the averaged momentum flux of the primary wave leads to the horizontal acceleration of the fluid with averaging assumed over at least a wavelength. It is generally assumed that this deposition of momentum leads only to the acceleration and establishment of an altered mean wind and a corresponding residual circulation via

$$\frac{\partial \bar{u}}{\partial t} \simeq -\frac{1}{\bar{\rho}} \frac{\partial(\bar{\rho} \overline{u'w'})}{\partial z} + f\bar{v}. \quad (1.1)$$

Average accelerations of $\sim (30 - 100)$ m/s/day have been inferred near the mesopause during summer and winter months in radar measurements and modeling studies (Fritts and Vincent, 1987; Reid and Vincent, 1987; Tsuda et al., 1990; Holton, 1983; Rind et al., 1988; Garcia and Solomon, 1985; Roble and Ridley, 1994; Huang and Smith, 1995; Hamilton et al., 1995; McLandress, 1998; Beagley et al., 1997). Hence, the effect of wave breaking on the mean circulation in the upper mesosphere and lower thermosphere is quite large. Although temporally and spatially localized body forces do create mean winds [which are time-independent responses and which may be broadened spatially (Vadas and Fritts, 2001a, hereafter VF; Vadas and Fritts, 2001b; Luo and Fritts, 1993; Zhu and Holton, 1987)], they also generate high and low-frequency secondary waves with potentially large momentum fluxes (VF). It turns out that for deep, 3D body forcings that arise from wave breaking and for which the width equals the length (along the body force), roughly one-quarter of the energy resides in secondary waves, while three-quarters of the energy drives the mean response (see Sec. 5b).

Here, we apply the linear model of VF to wave breaking in the mesosphere in order to characterize the secondary waves created from our “body force generation” mechanism. The purpose of our paper is to explore the characteristics of the secondary gravity waves that are created purely by the linear response to the deposition of momentum that occurs during 3D wave breaking. This represents a significant generalization of previous studies of the mean and wave responses to local body forcing by Zhu and Holton (1987), Fritts and Luo (1992), and Luo and Fritts (1993), all of which considered only impulsive or step-function momentum sources.

Such sources are distinct from those due to nonlinear interactions, for example the forcing of harmonics of the primary waves due to large amplitudes, the resonant triad interactions examined by McComas and Bretherton (1977), Yeh and Liu (1981), Dunkerton (1987), Klostermeyer

(1991), and Vanneste (1995) or the "envelope radiation" due to localized instabilities studied by Fritts (1984), Chimonas and Grant (1984), and Scinocca and Ford (2000). The present mechanism bears a closer resemblance to the model of envelope radiation advanced by Bühler et al. (1999) in which gravity waves are radiated by the altered and unbalanced thermal and wind fields accompanying shear instability and local heat and momentum transports. The present mechanism, however, arises from divergent momentum fluxes due to propagating waves and may occur across many spatial and temporal scales. Our model is not intended to parameterize all of the secondary waves generated from wave breaking; secondary waves generated from sub-wavelength-sized, nonlinear interactions are not accounted for in our model.

As shown in VF, secondary waves are efficiently created from temporally and spatially-localized body forcings and heatings. In order to study the simplest possible (and likely most important) case, we focus here on zonal body forcings. Meridional body forcings are also shown briefly to generate analogous secondary waves and momentum fluxes. Heat sources are not considered here. We first show that our linear model can explain some of the features of the secondary waves and zonal winds generated in the 2D nonlinear wave breaking model study by Holton and Alexander (1999a, hereafter, HA). We then apply our model to the most important case, body forcing from 3D wave breaking. We determine the wave characteristics and momentum fluxes associated with typical 3D body forces from wave breaking in the mesosphere.

We organize this paper as follows. In Sec. 2, we briefly summarize the pertinent results obtained from HA. In Sec. 3, we summarize our model and define various quantities of interest. In Sec. 4, we compare the secondary waves and zonal wind features from HA with our model. In Sec. 5, we explore the character of secondary waves from 3D body forcings. Sec. 6 contains a summary and discussion of our results.

2. Review of the nonlinear wave breaking study by HA

HA simulated a storm in a 2D cloud-resolving model (see Fig. 1). This storm generated primary gravity waves, which then propagated and broke in the mesosphere at $Z \simeq 75$ km. Shortly after breaking of the eastward primary waves began, the authors noted that secondary waves were observed moving downward and eastward. Positive and negative momentum flux masks (M^+ and M^- , respectively) were applied to the solution in order to separate the primary "up-going" waves from the secondary "down-going" waves. Fig. 9 of HA showed the vertical velocity power spectral densities for the waves with positive and negative momentum fluxes during wave breaking. The secondary waves had shorter periods and horizontal wavelengths than the peak in the primary wave spectrum. In the ground relative frame, the spectral peaks for the negative momentum ("down-going") waves occur at $\lambda_x \simeq 20$ km, $2\pi/\omega = 8$ min, and $c_x \simeq 40$ ms⁻¹, while the spectral peaks for the positive momentum ("up-going") waves occur at $\lambda_x \simeq 100$ km, $2\pi/\omega \simeq 50$ min, and $c_x \simeq 50$ ms⁻¹. Although the authors only noted the presence of downgoing-eastward waves, we note the possibility that upgoing-eastward, upgoing-westward, and downgoing-westward secondary waves were also created during wave breaking. Any upgoing secondary waves would be rapidly dissipated by the sponge, which was employed to damp out wave activity above 78 km. Any downgoing-westward waves would have positive momentum flux and might be included in HA's M^+ mask and "up-going" spectra. In fact, there are peaks with similar amplitudes at short wavelengths and high frequencies in both the "up-going" and "down-going" wave spectra. If the downgoing-westward secondary waves

are present then, they do not appear to be larger in amplitude than the downgoing-eastward secondary waves.

The Richardson number-dependent vertical diffusion coefficient inferred by HA is reproduced here in Figure 2. Strong, isolated patches of enhanced diffusion are seen at altitudes of 68 to 75 km and correspond to specific phases of the primary waves. Our current theoretical understanding of wave dissipation implies a momentum flux divergence which is averaged over some volume, presumably at least as large as a wavelength and as long as a period. We will examine the character of secondary waves emitted by such localized body forces and compare with the results of HA in Section 4.

Shortly after wave breaking begins, large-scale, eastward, zonal winds are generated in the wave breaking region. Fig. 1 shows contours of the zonal wind perturbation with respect to the storm frame at $t = 4$ hrs from the HA simulation. Two large patches of eastward zonal winds are located at $X = [800 - 1100]$ km and $Z \simeq 78$ km. These zonal wind features are ~ 6 km deep, 100 km wide, and have amplitudes (relative to the background wind at that height) of $u \sim 40 \text{ m s}^{-1}$. These wind features drifted westward and disappeared within an hour at a time when breaking of the westward propagating primary waves and the westward wind accelerations had become important. Our model comparison in Sec. 4 provides an explanation of the origin of these wind features.

3. Model discussion

a. Model summary and source profile

The VF model calculated the secondary wave generation and mean response to an idealized body force localized in time and space. Here, we use the term ‘mean’ to denote the time-independent portion of the response. VF derived the 3D, Boussinesq, analytic, linear solutions for body forces and heatings [Eqs. (3.8)-(3.17)]. The secondary waves are assumed not to interact with each other or with the mean flow. Mean shears are also neglected to permit an analytic formulation.^b The general response consists of a steady, time-independent mean flow and a gravity wave response. However, if the body force is steady in time, only a mean response arises. Therefore, it is important to appropriately model the temporal variability of the body force to obtain the correct secondary wave spectrum and momentum fluxes. We assume a representative altitude of $z_0 = 75$ km with $N^2 = 3.5 \times 10^{-4} \text{ s}^{-2}$. The zonal acceleration due to the body force is modeled as $F_x(\mathbf{x})\mathcal{F}(t)$, where $F_x(\mathbf{x})$ is the (arbitrary) spatial distribution and $\mathcal{F}(t)$ is the temporal distribution of the body forcing. Because wave breaking occurs intermittently within a wave field (Andreassen et al., 1994; LeLong and Dunkerton, 1998; Walterscheid and Schubert, 1990; HA; Franke and Robinson, 1999; Liu et al., 1999), body force regions will likely be spatially patchy, with widths and depths estimated to be of order a wavelength or more according to current theoretical understanding, depending on the coherency of the wave packet during wave breaking. In addition, body force durations will be of order or greater than a wave period.

For purposes of illustration, we approximate most of these body forcing regions (i.e.,

^bThe secondary wave spectrum in a sheared flow will evolve differently in time, with a portion of the spectrum experiencing critical levels which cannot be described in this analytic formulation. In addition, the generated gravity wave spectrum may be different in a sheared flow due to nonlinear interactions which cannot be taken into account in our linear formulation.

sources^{c)} as Gaussian monopoles:

$$F_x(\mathbf{x}) = u_0 \exp \left(-0.5 \left[\frac{(x - x_0)^2}{\sigma_x^2} + \frac{(y - y_0)^2}{\sigma_y^2} + \frac{(z - z_0)^2}{\sigma_z^2} \right] \right), \quad (3.1)$$

where u_0 is the body force strength, σ_x , σ_y , and σ_z are the source half widths at half maximum, and where (x_0, y_0, z_0) is the force location. The total spatial extents of the body force are approximately $4.5\sigma_x$, $4.5\sigma_y$, and $4.5\sigma_z$. Because the solution is linear, the secondary wave winds and potential temperatures are directly proportional to the forcing strength u_0 . The temporal evolution of the body force is assumed to have the form^{d)}

$$\mathcal{F}(t) = \frac{2}{\sigma_t} \begin{cases} \frac{1}{2}(1 - \cos \hat{a}t) & \text{for } 0 \leq t \leq \sigma_t \\ 0 & \text{for } t \geq \sigma_t, \end{cases} \quad (3.2)$$

where the forcing frequency is $\hat{a} \equiv 2\pi n/\sigma_t$, the force duration is σ_t , and the number of force cycles is n which we set to equal one here ($n = 1$) to represent that each individual body force is applied as a single pulse in time.

Body forces create secondary gravity waves with frequencies $\omega = \sqrt{(k_H^2 N^2 + m^2 f^2)/(k_H^2 + m^2)}$, where $\mathbf{k} = (k, l, m)$ and $k_H^2 = k^2 + l^2$. The Gaussian source has “characteristic” wavenumbers $k_c = 1/\sigma_x$, $l_c = 1/\sigma_y$, and $m_c = 1/\sigma_z$ with characteristic source frequency

$$\omega_c = \left[\frac{(\sigma_x^{-2} + \sigma_y^{-2})N^2 + \sigma_z^{-2}f^2}{\sigma_x^{-2} + \sigma_y^{-2} + \sigma_z^{-2}} \right]^{1/2}, \quad (3.3)$$

and with characteristic source period $\tau_c = 2\pi/\omega_c$. All body forces studied in this paper are “deep”, which means that $\omega_c \gg f$.

The spatial and temporal scales of the body force are based on the spatial and temporal scales of the breaking wave packet. The spatial scales are of order or larger than the primary wavelengths. And the body force duration is of order or larger than the primary wave period. Because τ_c is approximately the period of the breaking wave, our body force durations are chosen to be $\sigma_t = [1, 2]\tau_c$. As found from VF, fast/impulsive forcings occur over time scales much less than the characteristic period, while slow forcings occur over times scales much greater than the characteristic period. Forcings from gravity wave breaking, then, are reasonably fast and therefore result in secondary wave fluxes that are smaller than that from impulsive forcings, but are still large and potentially significant at higher altitudes. For most of the 3D examples shown in this paper, $\sigma_t \simeq 15 - 50$ minutes. This is consistent with observations (Fritts and Vincent, 1987), which show that most of the mean zonal momentum flux observed above 78 km at mid latitudes is due to waves with periods < 1 hour.]

Finally, we address the issue of spatial and temporal inhomogeneity within the body force region. In VF, we examined the generated secondary wave spectrum when temporal and spatial variability was added to a Gaussian body force patch, and we found the expected results; that higher frequency and shorter wavelength secondary waves are generated at the added temporal and spatial scales. Here, we do not include inhomogeneities at scales smaller than a wavelength

^{c)}Here, we define the source, which equals F_x , to be the spatial portion of the zonal body force.

^{d)}The quantity, σ_t , was referred to in VF as σ .

and temporal variance within a wave period, however. The body forces we consider are those due to the momentum flux divergence that results as a consequence of the breaking primary wave or wave packet and are obtained via spatial and/or temporal averaging, presumably over a primary wavelength and over a primary wave period. Therefore, the body force patches we consider in this paper are assumed to contain no sub-wavelength and sub-period variability, and are distinct and separate from other nonlinear mechanisms mentioned in the introduction. To represent the body forcing and secondary wave excitation due to breaking and dissipation in a complex wave field, we can superpose the (linear) responses to sources having various spatial extents and forcing durations and centered at different times (Vadas and Fritts, 2002).

b. Power spectral densities

The Fourier transform of the vertical velocity, \tilde{w} , is

$$\tilde{w}(k, l, m, t) = dx dy dz \sum_{i=1}^{N_x} \sum_{j=1}^{N_y} \sum_{k=1}^{N_z} e^{ikx_i + il y_j + im z_k} w(x_i, y_j, z_k, t), \quad (3.4)$$

where dx , dy , and dz are the grid point spacings, and N_x , N_y , and N_z are the number of grid points. The 3D power spectral density (PSD) of the vertical velocity, P_{klm} , is given by

$$P_{klm} = \frac{dx dy dz}{N_x N_y N_z} \tilde{w}_d \tilde{w}_d^*, \quad (3.5)$$

where the “*” is the complex conjugate. In addition, $\tilde{w}_d = \tilde{w}/(dx dy dz)$ is the discrete Fourier transform of the vertical velocity: $\tilde{w}_d = \sum_{i,j,k} e^{ikx_i + il y_j + im z_k} w(x_i, y_j, z_k)$. Using $dk = 1/dx N_x$, $dl = 1/dy N_y$, and $dm = 1/dz N_z$, Eq. (3.5) becomes $P_{klm} = dk dl dm |\tilde{w}|^2$. Using Parseval’s Theorem, the total power in the spectrum is therefore the power of the signal in physical space,

$$\sum_{klm} P_{klm} = \sum_{klm} dk |\tilde{w}|^2 = \sum_{ijk} d\mathbf{x} w(x_i, y_j, z_k)^2. \quad (3.6)$$

The 1D PSD for the vertical velocity is defined as

$$\text{PSD}_{ww^*} = \sum \frac{P_{klm} dk dl dm}{d\eta} = \frac{\int_{\sigma_t}^{\sigma_t + 2\pi/\omega} \tilde{w}_d \tilde{w}_d^* dt}{d\eta (N_x N_y N_z)^2 \int_{\sigma_t}^{\sigma_t + 2\pi/\omega} dt} \quad (3.7)$$

where the sum is over all quantities other than the binned quantity^e. Here, $d\eta$ is the interval length of the binned quantity (e.g., dm , dc_x , etc). We average over each gravity wave’s period in order to obtain the exact wave amplitudes from our spectral solutions. The PSD of the zonal velocity, PSD_{uu^*} , is obtained similarly by substituting u for w in Eq. (3.7). The zonal momentum fluxes (per unit mass) are similarly defined as

$$\text{PSD}_{uw^*}(k, l, m) = \frac{|\int_{\sigma_t}^{\sigma_t + 2\pi/\omega} \tilde{u}_d \tilde{w}_d^* dt| (1 - f^2/\omega^2)}{d\eta (N_x N_y N_z)^2 \int_{\sigma_t}^{\sigma_t + 2\pi/\omega} dt}. \quad (3.8)$$

Here, we add up the absolute value of the momentum fluxes in order to prevent the positive (e.g., eastward and upward) and negative (e.g., westward and upward) contributions from canceling

^eThe PSD is defined slightly differently here than in VF.

out for Gaussian, untilted body forces. A similar expression is defined for the meridional momentum fluxes, PSD_{vw^*} . All power spectral densities are in units of $(\text{m}^2\text{s}^{-2})/d\eta$.

c. Secondary wave momentum fluxes

The total momentum flux carried by secondary gravity waves is easily calculable in spectral space: $\sum_{klm} d\mathbf{k} \sqrt{|\tilde{u}\tilde{w}^*|^2 + |\tilde{v}\tilde{w}^*|^2}(1 - f^2/\omega^2)$. We compare this to the momentum flux deposited by the breaking gravity waves. Using the zonal-mean, Boussinesq expression, the zonal force is

$$F_x(\mathbf{x})\mathcal{F}(t) \simeq \frac{\partial}{\partial z}(\overline{u'w'})_{\text{break}}, \quad (3.9)$$

where $(\overline{u'w'})_{\text{break}}$ is the momentum flux of the breaking wave (Andrews et al., 1987). Thus, $(\overline{u'w'})_{\text{break}}$ evolves in time as $\mathcal{F}(t)$. Integrating from $t = 0$ to σ_t , noting that the change in momentum flux occurs over the depth of the body force, and integrating over physical space, the change in momentum flux of the primary breaking wave is

$$\sum_{i,j,k} d\mathbf{x} \Delta(\overline{u'w'})_{\text{break}} \sim \frac{4.5\sigma_z}{\sigma_t} \sum_{i,j,k} d\mathbf{x} F_x(x_i, y_j, z_k). \quad (3.10)$$

The fraction of the total momentum flux in the secondary waves compared to the change in momentum flux of the breaking wave is then approximately

$$\frac{\sigma_t \sum_{klm} d\mathbf{k} \sqrt{|\tilde{u}\tilde{w}^*|^2 + |\tilde{v}\tilde{w}^*|^2}(1 - f^2/\omega^2)}{4.5\sigma_z \sum_{ijk} d\mathbf{x} F_x}. \quad (3.11)$$

4. Comparison of secondary waves in HA with our model results

In this section, we examine the secondary wave and mean wind responses that are created by the body force generation mechanism within current theoretical understanding. Although the body force generation mechanism may account for some of the secondary gravity waves in HA, secondary waves are also likely created from nonlinear generation mechanisms which are unaccounted for in our model. The body forces should occur in the region where strong mixing (and wave dissipation) occurs in Fig. 2, and are estimated to be approximately the size of a primary wavelength vertically and horizontally. If the body forces are separated by at least their horizontal width, then the total secondary wave spectrum that results approximately equals the sum of the spectra for each individual body force (see Sec. 4b). We select two representative body forces based on the primary wavelength variation in Fig. 2, cases I and II, in Table 1. The depths in Table 1 refer to the full depths, which are approximately twice the full depth at half-maximum. The same applies for the widths. The body forces from the region that case I represents (i.e., $X \simeq 1100 - 1300$ km) are likely untilted (because of the high primary wave frequency). The body forces from the region that case II represents (i.e., $X \simeq 1300 - 1500$ km) are likely tilted (because of the lower primary wave frequency). The zonal acceleration during wave breaking averaged over the eastern half of the domain was $\simeq 700$ m/s/day at $Z = 75$ km (Fig. 11b of HA). Because wave breaking only occupied half of this longitudinal extent, and assuming that the body forces only occupy $\sim 1/8 - 1/2$ of the area within this region (Fig. 2), the spatially-localized, individual body force accelerations are estimated to be $2800 - 10^4$ m/s/day for very short time intervals. The force durations are chosen from Sec. 3a. Cases I and II are modeled here with $f = 0$. Because the force strengths are so large, nonlinear secondary

Table 1: Test case parameters for 2D Gaussian forces

case #	$\sigma_z =$	$\sigma_x =$	$u_0 =$	$\tau_c =$	n	depth \simeq	width \simeq
I	1.8 km	4.4 km	200 m/s	15 min	1	8 km	20 km
II	1.8 km	13 km	200 m/s	41 min	1	8 km	60 km

wave-wave and secondary wave-mean effects that we neglect here could also be important (see Appendix A), but likely would not prevent large scale secondary waves from being generated from the body force mechanism.

a. Test case studies

In Fig. 3, we show the zonal and vertical winds that result from case I.^f The secondary gravity waves propagate away from the body force in all four quadrants symmetrically, due to the lack of shear and background mean wind. [An asymmetry results when there is a background wind relative to the source (Fovell et al., 1992).] It is observed that the waves have frequencies that are of order or less than ω_c . For comparison purposes, we calculate the secondary wave amplitudes while the waves are still in the force region. At $t = 6$ min and for this forcing amplitude, the maximum vertical winds of the high-frequency secondary waves are 4.0 ms^{-1} (not shown). This is within the range of vertical velocities observed in HA of $\sim 2 - 16 \text{ ms}^{-1}$ (Fig. 7b of HA). In addition, the maximum zonal wind at this time and for this forcing amplitude is $u_{\text{max}} = 33 \text{ ms}^{-1}$, which is similar to $u \sim 40 \text{ m s}^{-1}$ of HA (see Sec. 2).

In Figs. 4 and 5, we show the vertical wind PSD for cases I and II, respectively. Here, the horizontal phase speed is $c_x = \omega/k = N/\sqrt{m^2 + k^2}$. The momentum deposited for each example in Figs. 4 and 5 is the same. The maxima and their locations depend sensitively on the force duration. For the $\sigma_t = \tau_c$ forcing, the peak frequency is somewhat smaller than ω_c and the vertical wavelengths are somewhat larger than twice the depth of the forcing. The maxima amplitudes decrease, the peak frequency decreases, the horizontal wavelength increases, and the vertical wavelength decreases when the duration doubles to $\sigma_t = 2\tau_c$. The spectra in Figs. 4 and 5 represent secondary wave properties in the frame of reference moving with the body force. In Fig. 9 of HA, the spectra shown are in a frame stationary relative to the ground, and the body forces could be moving eastward relative to this frame. This uncertainty in the frame of reference means we must be cautious comparing the frequency and phase speed spectra here and in HA. However, we can tentatively compare the horizontal wavelength spectra between our model and HA because these spectra will not depend on the reference frame. Additionally, because of the uncertainty in the body force amplitudes, it is important to compare the location of the maxima rather than the PSD amplitudes in the horizontal wavelength spectra of Figs. 4 and 5. For the shorter force durations, the response in case I peaks at horizontal wavelengths of $\lambda_x \simeq 100 \text{ km}$ while the response in case II peaks at larger horizontal scales, $\lambda_x \simeq 270 \text{ km}$. Longer force durations yield secondary waves with even larger horizontal wavelengths. Thus the dominant horizontal wavelength is approximately four times the body force width. (We

^fUnless noted otherwise, $dx = \sigma_x/2$, $dy = \sigma_y/2$, and $dz = \sigma_z/2$ for all of the illustrations. This allows for 81 and 729 grid points within the force area for a 2D and 3D Gaussian monopole, respectively.

found previously that the dominant horizontal wavelength is only twice the body force width for impulsive forcings (VF).) Although the case I body forces generate secondary waves with horizontal wavelengths that are closer to those observed in HA than the case II body forces, still the horizontal wavelengths are too large. If the body force mechanism is responsible for most of the high frequency secondary waves observed in HA, then the dominant body forces in HA would have to be approximately $\simeq 10$ km across and have some sub-period temporal variability. This spatial scale is sub-wavelength-sized and similar to the size of the diffusivity patches in the region $X \simeq 1100 - 1300$ km of Fig. 2. It is not currently accepted that body forces can occur on sub-wavelength and sub-period scales, however.

HA found that the ratio of the momentum flux in the downgoing-eastward (M^-) waves to that of the primary (M^+) waves was 15-20%. We assume that nearly all of the primary wave momentum flux is deposited during wave breaking. (If the primary wave only loses a fraction of its momentum flux, or if downgoing-westward and/or upgoing secondary waves are also present in HA, then this comparison should be revised.) Using Eq. (3.11), the total fractional radiated momentum flux for case I is 29% and 19% for $\sigma_t = \tau_c$ and $2\tau_c$, respectively. Comparable numbers are obtained for case II. Therefore, as much as $\sim 7\%$ of the primary wave momentum flux is carried by secondary waves per quadrant (e.g., upward and eastward) in our model.

b. Effects of tilted, slanted, and multiple body forces

Because the primary waves break along phase lines, some of the body forces in HA may be tilted. This effect is especially likely for those body forces arising from the dissipation of waves with lower frequencies and larger horizontal wavelengths in the eastern portion of Fig. 2. In addition, multiple forces are created at the same time and are spread out horizontally and vertically due to intermittency of wave breaking within the wave field and superposition of waves within the wave packet. We model a body force tilted by ψ degrees via replacing x and z in Eq. (3.1) by $x' = x \cos \psi + z \sin \psi$ and $z' = -x \sin \psi + z \cos \psi$, respectively. Fig. 6a-c shows the secondary waves from a tilted, case II force. The horizontally-thin appearance in (a) occurs because the lengths of the horizontal and vertical axes in the plot are not the same. The secondary waves are created predominantly in the direction of the tilt, as noted previously (Fovell et al., 1992). Here, 76% of the momentum flux is positive. But only secondary waves with negative momentum flux were readily observed in HA, and even if secondary waves with positive momentum flux were created in HA, they were likely not greater in magnitude than the waves with negative momentum flux (see Sec. 2). Therefore, if body forces created some of the high-frequency, secondary waves in HA, we conclude that they are likely untilted.

Fig. 6d shows two untilted, case I forces that are arranged on a slant (following lines of constant phase of the primary wave) and are separated horizontally by their width and vertically by their depth. Fig. 6e-f shows the secondary waves. This body force configuration produces only a small enhancement of gravity waves with positive momentum flux; 56% of the total momentum flux is positive. Larger body force separation distances decrease even this small enhancement, because the secondary waves from the body forces interact even more incoherently. Asymmetry in the spectrum of waves can also be related to mean wind effects (e.g., Fovell et al., 1992; Pfister et al., 1993).

Fig. 7 shows the secondary wave spectra for three case I forces that are equally spaced horizontally by separation lengths ranging from 0 to $3\mathcal{D}_x$, where $\mathcal{D}_x \equiv 4.5\sigma_x$ is the horizontal

diameter of each force. (The separation length is the horizontal distance that separates the force centers.) For separation lengths greater than or equal to $2\mathcal{D}_x$, the main component of each spectrum peaks at the same frequency as that for a single force. For the separation length of \mathcal{D}_x (where the forces are touching), however, the peak frequency is a few times smaller than ω_c because of the coherent nature of the extended force. Thus, if body forces are separated by more than their width, the secondary wave spectra will be approximately the sum of the spectra for each body force. Note that all spectra peak at vertical wavelengths which are about twice the depth of the force (not shown).

c. Generated low-frequency zonal waves

A 2D latitudinally-symmetric body force does not create a strictly time-independent, mean response (VF). It does create low-frequency waves, however, as was seen in Fig. 3 for a case I body force. These low-frequency waves have periods greater than a few hours and propagate horizontally away from the force region with a velocity field which expands in time.^g This response may resemble zonal mean winds, because these waves have large horizontal scales and periods. The vertical extent of each wave packet is the depth of the body force, which is $\simeq 8$ km here. Due to wave dispersion, their horizontal size increases in time and their amplitude decreases. At $t \simeq 30$ and 100 min, each packet is ~ 130 and ~ 610 km across, respectively, which are much larger than the horizontal extent of the body force. The case II body force produces similar low-frequency waves.

In HA, eastward zonal winds were observed propagating westward away from the wave breaking region (see Sec. 2). We believe these winds are similar to the low-frequency gravity waves created from the body force generation mechanism. These observed wave packets were ~ 6 km deep, ~ 100 km wide, and had amplitudes relative to the background wind of $u \sim 40 \text{ ms}^{-1}$ (Fig. 1), which is similar to our model results. These winds in HA might also be the superposition of low-frequency waves from several, simultaneously-occurring body forces. Thus the large amplitude, large horizontal scale, low-frequency zonal winds present in HA signal that the body force generation mechanism was likely present during HA; this is the natural conclusion, because momentum was deposited during wave breaking. Because body forces were likely present during HA, and because the body force mechanism also creates high-frequency waves, it is likely that some of the high-frequency secondary waves in HA were generated by the body force mechanism. It is also possible that the body force mechanism created some of the secondary waves observed in the 2D models of Bacmeister and Schoeberl (1989), Satomura and Sato (1999), Franke (1996), and Franke and Robinson (1999), although we do not have sufficient information to test these postulates.^h

In conclusion, the simple, linear body force generation mechanism may explain some of the features from HA's 2D wave breaking simulation; highly localized body forces may be responsible for some of the observed secondary waves (low and high frequency). We now explore the most important case: the ramification of the body force mechanism in 3D.

5. 3D body forces from wave breaking

^gThese low-frequency waves are not inertia-gravity waves, since $f = 0$.

^hThose 2D simulations with horizontal domains of only a single, horizontal, primary wavelength can not properly examine these low-frequency waves because their horizontal domain is too small.

a. General characteristics

Wave breaking in 3D results in deposition of some or all of the momentum flux carried by the primary wave. Depending on the nature of wave breaking and the character of the primary wave field, regions of body forcing may vary from the scale of the primary wave horizontal and vertical wavelengths to the scale of the primary wave packet, which may be many times larger, according to current theory. In addition to a mean response, a localized body force generates upward and downward-propagating secondary gravity waves. The generation of secondary waves is equally effective at mid latitudes and at the equator for a deep force (i.e., $\omega_c \gg f$) of reasonably short duration (including $\sigma_t \simeq \tau_c$), provided there is significant spatial variation in the direction of the force [see Eqs. (5.8) and (5.23) below]. We note, however, that the spatial and temporal characteristics of the body forces created near the mesopause from wave breaking may differ at differing latitudes and longitudes due to different primary wave source mechanisms (e.g., tropic storms, mountain waves, etc). From Eqs. (3.13)-(3.15) of VF, the post-forcing, temporally-averaged gravity wave velocities and momentum fluxes for zonal body forcings in an environment with no background wind are

$$\overline{|\tilde{u}_{\text{GW}}|^2} = \xi \zeta [k^2(N^2 - \omega^2) + m^2 f^2]^2 \quad (5.1)$$

$$\overline{|\tilde{v}_{\text{GW}}|^2} = \xi \zeta [k^2 l^2 (N^2 - \omega^2)^2 + m^4 f^2 \omega^2] \quad (5.2)$$

$$\overline{|\tilde{w}_{\text{GW}}|^2} = \xi \zeta m^2 \omega^2 (k^2 \omega^2 + l^2 f^2) \quad (5.3)$$

$$\overline{\tilde{u}_{\text{GW}} \tilde{w}_{\text{GW}}^*} = -\xi \zeta m k \omega^2 [k^2 (N^2 - \omega^2) + m^2 f^2] \quad (5.4)$$

$$\overline{\tilde{v}_{\text{GW}} \tilde{w}_{\text{GW}}^*} = -\xi \zeta m l \omega^2 [k^2 (N^2 - \omega^2) + m^2 f^2], \quad (5.5)$$

where the overline represents the temporal average over each wave's period, where the subscript "GW" refers to the gravity wave portion of the solution, and where

$$\xi = \frac{4\hat{a}^4 \sin^2(\omega\sigma_t/2)}{(\hat{a}^2 - \omega^2)^2 \omega^2 \sigma_t^2}, \quad (5.6)$$

$$\zeta = \frac{|\tilde{F}_x|^2}{2[(k^2 + l^2)N^2 + m^2 f^2]^2}. \quad (5.7)$$

Eq. (5.6) equals one for fast/impulsive forces, and equals 1/4 for $\sigma_t = \tau_c$ at $\omega = \omega_c$. Fig. 8 shows ξ for several values of σ_t . Only the $\sigma_t \geq \tau_c$ cases are relevant for the body force mechanism as arising from gravity wave breaking. Because the spatial portion of the forcing peaks approximately at ω_c , for forcing durations appropriate to body forcing from wave breaking, the high-frequency end of the secondary gravity wave spectrum is cut-off.

Changing the latitude of the body force alters negligibly the secondary wave momentum flux spectrum when this body force is deep and has $k_c^2(N^2 - \omega_c^2) \gg m_c^2 f^2$, or

$$\sigma_x/\sigma_z \ll \sqrt{1 - \omega_c^2/N^2} N/f. \quad (5.8)$$

When $\omega_c \lesssim N/2$, this condition is $\sigma_x/\sigma_z \ll 200$ at mid latitudes and $\sigma_x/\sigma_z \ll 140$ at high-latitudes. For example, for 3D body force geometries that are determined by source conditions, i.e., convection or orography, typical body force widths and depths are likely to be $4.5\sigma_x \sim 5 - 100$ km, $\sigma_y \gtrsim \sigma_x$ (i.e., $4.5\sigma_y \sim 5 - 1000$ km), and $4.5\sigma_z \sim 5 - 15$ km. (The depth is

the full depth, which is approximately twice the full depth at half-maximum. Similarly for the full width.) For these 3D, deep body forces, the secondary wave momentum flux spectra are insensitive to latitude. In addition, the energy in secondary waves for these body forces are comparable to the energy in the mean responses (VF). This result is in stark contrast to the result from deep, zonally-symmetric, zonal body forcings, for which 1) the secondary wave spectra are very sensitive to latitude (e.g., there are *no* secondary waves for body forces near the equator), and 2) even though secondary waves are generated for body forces at mid and high latitudes, their energy and associated momentum fluxes are very small (see below). The reason these zonal body force situations are so different is that for zonally-symmetric, zonal body forces, the only restoring force is the Coriolis torque, which results in geostrophic adjustment. But geostrophic adjustment is an inefficient generator of high-frequency, secondary waves due to its long temporal scale. However, when a body force has significant spatial variation in the direction of the force, the gravitational force is the dominant restoring force, acts on buoyancy time scales, and allows for the efficient generation of high-frequency waves if those frequencies are important in the body force spectrum.

It is accepted that breaking gravity waves cause the reversal of the jets in the summer and winter mesosphere by applying a mean acceleration of $\sim 100\text{m/s/day}$ (Fritts and Vincent, 1987; Reid and Vincent, 1987; Tsuda et al., 1990; Holton, 1983; Rind et al., 1988; Garcia and Solomon, 1985; Roble and Ridley, 1994; Huang and Smith, 1995; Hamilton et al., 1995; McLandress, 1998; Beagley et al., 1997). For dissipation depths of a scale height, this requires daily mean gravity wave momentum fluxes of $\sim 10\text{ m}^2\text{s}^{-2}$ (Fritts and Yuan, 1989; Fritts et al., 1992). However, gravity wave breaking also occurs sporadically in time. For example, momentum fluxes as large as $\sim 60\text{ m}^2\text{s}^{-2}$ for hourly intervals have been measured by radar (Fritts and Yuan, 1989; Reid et al., 1988; Fritts et al., 1992), while estimates derived from airglow measurements of Yamada et al. (2001) may be as large as $\sim 50 - 200\text{ m}^2\text{s}^{-2}$ (Fritts et al., 2002). We estimate the strength of a body force to be [see Eq. (3.10)]: $\Delta(\overline{u'w'})_{\text{break}}\sigma_t/L_z$, where L_z is the depth over which dissipation occurs. For events of 1hr duration and $L_z \sim H$ in depth, $\Delta(\overline{u'w'})_{\text{break}} \sim 50 - 200\text{ m}^2\text{s}^{-2}$ yields body force strengths of $\sim 25 - 100\text{ ms}^{-1}$. These larger events will have correspondingly larger radiation of secondary waves and momentum fluxes. More conservative flux values of $\sim 20 - 40\text{ m}^2\text{s}^{-2}$ imply body force strengths of $\sim 10 - 20\text{ ms}^{-1}$. For the illustrations in this section, we choose a strength of 30 ms^{-1} as representative of the stronger forcing events likely to play a greater role in secondary wave radiation. This implies a maximum force strength of $u_0 = 60\text{ ms}^{-1}$.

The zonal and meridional momentum fluxes (per unit mass) at (k, l, m) with spectral resolution dk , dl , and dm are

$$M_{uw} = \frac{\tilde{u}_{\text{GW}}\tilde{w}_{\text{GW}}^*(1 - f^2/\omega^2)dkdl dm}{\int \int \int (F_x/u_0)d\mathbf{x}} \quad (5.9)$$

$$M_{vw} = \frac{\tilde{v}_{\text{GW}}\tilde{w}_{\text{GW}}^*(1 - f^2/\omega^2)dkdl dm}{\int \int \int (F_x/u_0)d\mathbf{x}}, \quad (5.10)$$

respectively. Because an untilted Gaussian force excites symmetric (but not equal) zonal and meridional momentum fluxes, the positive and negative contributions are accounted for separately. The total zonal and meridional momentum fluxes are $\int |M_{uw}|$ and $\int |M_{vw}|$, respectively. The total momentum flux is $\int \sqrt{M_{uw}^2 + M_{vw}^2}$.

b. Body forces with similar horizontal extents

In this section, we study the wave and mean responses to 3D body forces with equal horizontal extents. From Eqs. (5.1)-(5.5), a deep body force with equal horizontal extents excites high-frequency, secondary waves with

$$\overline{|\tilde{u}_{\text{GW}}|^2} \simeq \overline{|\tilde{v}_{\text{GW}}|^2} \simeq \xi \frac{|\tilde{F}_x|^2}{8}, \quad (5.11)$$

$$\overline{|\tilde{w}_{\text{GW}}|^2} \simeq \xi \frac{|\tilde{F}_x|^2}{4} \left(\frac{\omega}{N}\right)^2, \quad (5.12)$$

$$\overline{\tilde{u}_{\text{GW}}\tilde{w}_{\text{GW}}^*} \simeq \overline{\tilde{v}_{\text{GW}}\tilde{w}_{\text{GW}}^*} \simeq -\xi \frac{|\tilde{F}_x|^2}{2^{5/2}} \left(\frac{\omega}{N}\right), \quad (5.13)$$

where we set $k = l$, $f \simeq 0$, and $\omega \ll N$. Thus, the horizontal wind spectra reflect the spatial attributes of the force, while the vertical wind and momentum flux spectra are accentuated somewhat by waves with $\omega > \omega_c$, depending on the force duration. In addition, up to one-quarter of the energy resides in the gravity wave response [see Eq. (5.20) below], depending on the force duration.

In Fig. 9, we show the mean and wave responses to a body force that is 100km wide and 20 km deep. (The width and depth refer to the full width and full depth, or $4.5\sigma_x$, $4.5\sigma_y$, and $4.5\sigma_z$.) The induced zonal mean wind closely resembles the body force, and has a maximum amplitude of $\bar{u} \sim u_0/2 = 30 \text{ ms}^{-1}$. Significant generation of secondary waves also occurs. These propagate away from the force region symmetrically. The integrated, upward momentum flux in the secondary wave field is $5.9 \text{ m}^2\text{s}^{-2}$. (The downward flux equals the upward flux, but will likely be unimportant relative to other waves at lower altitudes.) The upward, eastward (or westward) momentum fluxes are $2.7 \text{ m}^2\text{s}^{-2}$, while the upward, northward (or southward) momentum fluxes are $1.3 \text{ m}^2\text{s}^{-2}$. Fig. 10 shows the resulting secondary wave momentum fluxes above the body force. The secondary waves are focused in the direction of the body force, which is zonal here. The waves are located roughly along a cone that emanates from the body force and spreads away from the body force in the direction of the force with angle $\sin^{-1}(\omega_c/N)$ with respect to the vertical. Fig. 11a shows the momentum flux spectrum for a single quadrant (e.g., upward and eastward, northward and southward) for the body force in Fig. 9. Although the peak in the spectrum occurs at somewhat less than both the characteristic frequency and twice the depth of the body force, there is substantial momentum flux at vertical wavelengths as large as $\sim 60 - 100 \text{ km}$. In addition, a substantial amount of waves have horizontal phase speeds as large as $c_x \sim 200 \text{ ms}^{-1}$ and vertical group velocities as large as $|c_{gz}| \sim 30 - 60 \text{ ms}^{-1}$. Thus, if this force was created from a primary wave with a vertical wavelength of $\sim 10 \text{ km}$, significant generation of secondary waves with much larger vertical wavelengths and phase speeds would occur. The waves with large phase speeds would have a greater potential for surviving mesopause and lower thermosphere wind shears and propagating well into the thermosphere. As these waves propagate upwards into realistic winds, the waves with positive and negative momentum flux will dissipate at differing altitudes depending on their differing intrinsic phase speeds. This spectrum would therefore provide a variable influence on the lower and middle thermosphere with altitude. Fig. 11b shows that the Earth's rotation does not significantly influence the secondary wave spectrum, as predicted by Eq. (5.8).

Fig. 12 shows the momentum flux in a single quadrant for the same body force as in Fig. 9 but having differing force durations. Only the $\sigma_t = \tau_c$ and $2\tau_c$ cases are relevant for the body force mechanism as arising from gravity wave breaking. The shorter-duration forcing is shown to illustrate which portion of the spectrum is lost for the longer force durations associated with this mechanism. Although the low-frequency, short λ_z portions of the spectra are the same for all cases, the high-frequency, large λ_z portions of the spectra are cut-off as the force duration lengthens. The total upward, integrated momentum fluxes are $15\text{m}^2\text{s}^{-2}$, $6\text{m}^2\text{s}^{-2}$, and $2\text{m}^2\text{s}^{-2}$, for $\sigma_t = 0.5\tau_c$, τ_c , and $2\tau_c$, respectively. The meridional momentum fluxes are approximately half of the zonal momentum fluxes for these zonal body forces.

Fig. 13 shows the frequencies and wavelengths having the peak momentum fluxes for differing force widths (diamonds and triangles) and differing force durations, but having the same depth as in Fig. 9. The gravity wave peak and width characteristics reflect both the temporal and spatial attributes of the body force. For $\sigma_t \geq \tau_c$, the cases relevant for the body force mechanism as arising from gravity wave breaking, the peak frequency is smaller than ω_c , the peak horizontal wavelengths are greater than twice the width of the body forces, and the peak vertical wavelength is somewhat less than twice the depth of the body force. However, there is a significant spread in these spectra to greater and smaller values (hatched lines). For example, although the peak vertical wavelength is $\simeq 30$ km, a large portion of momentum flux resides in waves with vertical wavelengths of 40 – 60 km. We emphasize that the secondary waves having large vertical wavelengths have a higher probability of reaching much higher altitudes.

As in 2D, some of the 3D body forces may be tilted with respect to the vertical along the phase lines of the primary breaking wave. In Fig. 14, we show the upgoing momentum flux for the same body force as in Fig. 9 but which is tilted 14 degrees zonally with respect to the vertical. As in 2D, the zonal momentum flux spectrum is in the direction of the tilt (see Fig. 6c). There is no anisotropy in the meridional momentum flux spectrum, as expected.

c. Body forces with unequal horizontal extents

In this section, we study the wave responses to 3D body forces with unequal horizontal extents. We find that the alignment direction of the shortest horizontal extent makes an enormous difference on the secondary wave momentum fluxes from deep forces. If the shortest horizontal dimension is in the direction of the body force, then the resulting secondary wave momentum fluxes are *much* larger than if the shortest horizontal dimension is normal to the body force (see also Sec. 5f). This dependence on the body force alignment occurs because of the different restoring forces that operate in each case, as discussed in Sec. 5a. As we will see, in the former case most of the energy resides in the wave response, while in the latter case most of the energy resides in the mean response.

For 2D, latitudinally-symmetric, deep zonal forces, the momentum flux is weighted toward frequencies of order ω_c :

$$\overline{|\tilde{u}_{\text{GW}}\tilde{w}_{\text{GW}}^*|} \simeq \xi \frac{|\tilde{F}_x|^2}{2} \frac{\omega}{N}, \quad (5.14)$$

where we set $l = 0$, $f = 0$, and $\omega \ll N$ in Eq. (5.4). For 2D, zonally-symmetric, deep zonal forces, however, the momentum flux is weighted toward inertial frequencies, with an amplitude

suppression of f/N :

$$\overline{|\tilde{v}_{\text{GW}}\tilde{w}_{\text{GW}}^*|} \simeq \xi \frac{|\tilde{F}_x|^2 f f}{2 N \omega}, \quad (5.15)$$

where we set $k = 0$ and $\omega \ll N$ in Eq. (5.5).

Fig. 15 shows the momentum flux spectra from zonally-symmetric and latitudinally-symmetric body forces that are 20km deep and 100km wide. The secondary wave momentum fluxes from the zonally-symmetric force is ~ 250 times smaller than that from the latitudinally-symmetric force at mid latitudes. We also show the spectrum for a 3D body force that is 20km deep and 100km wide in both the zonal and meridional directions. Its spectrum is similar to that from the 2D latitudinally-symmetric force. The total, upward secondary momentum fluxes at mid latitudes are $\sim 0.1 \text{ m}^2\text{s}^{-2}$, $\sim 13 \text{ m}^2\text{s}^{-2}$, and $\sim 6 \text{ m}^2\text{s}^{-2}$, for the zonally-symmetric, latitudinally-symmetric, and 3D body force, respectively.

In order to estimate the momentum fluxes excited by a zonal body force, we assume that the characteristic wavenumber and frequency are the dominant peaks in the spatial portion of the body force spectrum with negligible spread. (This is similar to the analysis performed in VF for estimating the maximum mean wind and thermal responses, as well as the fraction of energy in secondary waves.) This assumption is valid for the Gaussian body force. Evaluating Eqs. (5.4)-(5.5) at the characteristic wavenumber and frequency for deep, 3D body forces that satisfy Eq. (5.8), the peak momentum fluxes are estimated to be

$$\overline{\tilde{u}_{\text{GW}}\tilde{w}_{\text{GW}}^*} \sim \xi \frac{F_x(\mathbf{x})_{\text{max}}^2}{2} \left[\frac{k_c^3}{(k_c^2 + l_c^2)^{3/2}} \right] \frac{\omega_c}{N} \quad (5.16)$$

$$\overline{\tilde{v}_{\text{GW}}\tilde{w}_{\text{GW}}^*} \sim \xi \frac{F_x(\mathbf{x})_{\text{max}}^2}{2} \left[\frac{k_c^2 l_c}{(k_c^2 + l_c^2)^{3/2}} \right] \frac{\omega_c}{N}, \quad (5.17)$$

where ξ is evaluated at $\omega = \omega_c$, and where we set $\omega_c \ll N$. In addition, the maximum strength of the zonal body force is denoted $F_x(\mathbf{x})_{\text{max}}$, and equals u_0 for a Gaussian body force. We define α_{uw} and β_{vw} as

$$\alpha_{uw} \equiv \frac{2 \overline{\tilde{u}_{\text{GW}}\tilde{w}_{\text{GW}}^*} N}{\xi F_x(\mathbf{x})_{\text{max}}^2 \omega_c} \simeq \left[\frac{k_c^3}{(k_c^2 + l_c^2)^{3/2}} \right] \simeq \begin{cases} 1 & \text{for } \sigma_x \ll \sigma_y \\ (\sigma_y/\sigma_x)^3 & \text{for } \sigma_y \ll \sigma_x. \end{cases} \quad (5.18)$$

$$\beta_{vw} \equiv \frac{2 \overline{\tilde{v}_{\text{GW}}\tilde{w}_{\text{GW}}^*} N}{\xi F_x(\mathbf{x})_{\text{max}}^2 \omega_c} \simeq \left[\frac{k_c^2 l_c}{(k_c^2 + l_c^2)^{3/2}} \right] \simeq \begin{cases} \sigma_x/\sigma_y & \text{for } \sigma_x \ll \sigma_y \\ (\sigma_y/\sigma_x)^2 & \text{for } \sigma_y \ll \sigma_x. \end{cases} \quad (5.19)$$

Here, α_{uw} and β_{vw} are dimensionless, have maximum values equal to one, and are proportional to the magnitudes of zonal and meridional momentum fluxes, respectively, that a zonal body force has based on its horizontal dimensions. When the zonal extent of a body force is shorter than the meridional extent (for a zonal body force), the zonal momentum fluxes are much larger than the meridional momentum fluxes. When the meridional extent is shorter than the zonal extent, the meridional momentum fluxes are larger than the zonal momentum fluxes. In the former case, the momentum fluxes are large: $0.5\xi F_x(\mathbf{x})_{\text{max}}^2 (\omega_c/N)$. In the latter case, however, for the same ω_c and force strength, the momentum fluxes are much smaller: $0.5\xi F_x(\mathbf{x})_{\text{max}}^2 (\omega_c/N) (\sigma_y/\sigma_x)^2$. This difference occurs because in the former case, the secondary

wave energy dominates the total energy, whereas in the later case, the secondary wave energy is only a small fraction of the total energy. This is obtained from the estimated fraction of energy in secondary waves for deep, 3D zonal forces that satisfy Eq. (5.8), as obtained from Eq. (5.8) of VF:

$$\frac{E_{\text{GW}}}{\overline{E} + E_{\text{GW}}} \simeq \frac{\xi k_c^2}{\xi k_c^2 + l_c^2} \simeq \begin{cases} 1 & \text{for } \sigma_x \ll \sigma_y \\ \xi(\sigma_y/\sigma_x)^2 & \text{for } \sigma_y \ll \sigma_x, \end{cases} \quad (5.20)$$

where we have taken $\omega_c \ll N$. Here, E_{GW} and \overline{E} are the secondary gravity wave and mean energies, respectively. We illustrate these effects in Fig. 16. For a fixed ω_c and a fixed force strength, the total momentum fluxes are comparatively smaller when $\sigma_y \ll \sigma_x$ (i.e., when the mean energy dominates) as compared to when $\sigma_x \lesssim \sigma_y$. We overlay in (b) a quantity proportional to the total momentum flux, $\sqrt{\alpha_{uw}^2 + \beta_{vw}^2}$ (triangles), in order to show that the total momentum flux is proportional to the secondary wave energy. Because of energy conservation then, the largest secondary wave momentum fluxes are created from body forces which generate small mean responses.

Fig. 17a shows the contours of a deep, 3D zonal body forcing for which the zonal extent is the shortest horizontal extent: 100 km (zonal) \times 1000 km (meridional) \times 20 km (deep). This type of body force might be expected from mountain wave breaking, where the mountain is a north-south chain (e.g., the Rockies). The momentum flux spectrum is peaked at $\lambda_z \sim 35$ km and $2\pi/\omega \sim 42$ min, although significant flux is associated with waves having $\lambda_z \sim 50 - 100$ km. The total upward momentum flux is $9 \text{ m}^2\text{s}^{-2}$. For this orientation, 78% of the secondary energy resides in the waves. Fig. 17c shows the contours of the zonal force in (a), but rotated horizontally by 90 degrees. The meridional extent is now the shortest horizontal extent of the zonal body force. The resultant momentum flux spectrum is peaked at larger vertical wavelengths but at smaller frequencies. The total upward momentum flux is *much* smaller, $1.0 \text{ m}^2\text{s}^{-2}$, because most of the energy resides in the mean response. (In this case, only 7% of the energy resides in the secondary waves.) Thus, the orientation of a body force has a large impact on the resultant secondary wave spectra and momentum fluxes.

d. Multiple body forces

Fig. 18 shows the zonal wind spectra for three 3D body forces that are equally spaced zonally by separation lengths ranging from 0 to $3\mathcal{D}_x$, where $\mathcal{D}_x \equiv 4.5\sigma_x$ is the horizontal extent of each force. In (a), $\sigma_y = \sigma_x$, whereas in (b), $\sigma_y = 10\sigma_x$. For the separation length greater than or equal to $2\mathcal{D}_x$, the spectral peaks are very similar to that for each individual body force. Therefore, if multiple body forces are separated by more than their width, the resulting secondary wave spectra are approximately the same as the sum of the spectra for each individual body force.

e. Importance of spatial variability

From Eq. (3.3), $\omega_c \simeq \sqrt{2}N\sigma_z/\sigma_x$ for deep, 3D body forces where the horizontal extents are equal; the frequency of the wave response depends on the vertical to horizontal aspect ratio of the body force. Secondary wave wavelengths are determined by the spatial extents of the body force (Secs. 5b-c). Therefore if multiple body forces are averaged horizontally (due to numerical modeling constraints, say), then ω_c decreases. Thus horizontally averaged body forces create artificially smaller frequency and larger horizontal wavelength secondary waves

than would be created from the spatially unaveraged body forces. Additionally, horizontal averaging results in smaller force strengths; this leads to quadratically smaller secondary wave momentum fluxes, as was explored in Vadas and Fritts (2001b) for 2D body forces. In Fig. 19a, we show 16 3D body forces that are separated by their diameter horizontally. Each individual force is the same as in Fig. 9. In (b), we show the body force in (a) on a latitudinal-vertical slice at $y - y_0 = 100\text{km}$ and $z = z_0$. In addition, we show the same body force as in (a) but where the force is averaged horizontally using different window sizes ranging from 50 to 150 km wide. The resulting secondary wave momentum flux spectra are shown in (c). Although the total momentum deposited is the same for each distribution, the total upward secondary wave momentum fluxes vary substantially and are $5.3\text{m}^2\text{s}^{-2}$, $3.8\text{m}^2\text{s}^{-2}$, $2.1\text{m}^2\text{s}^{-2}$, and $1.1\text{m}^2\text{s}^{-2}$ for the unaveraged and averaged (by 50, 100, and 150 km) body forces, respectively. Thus horizontal averaging can significantly decrease the secondary wave momentum fluxes for deep forces. Therefore, it is necessary to retain the spatial variability of the wave breaking region in order to correctly estimate the secondary wave properties and associated momentum fluxes.

f. Meridional body force

In this paper, we showed the responses to zonal body forces only for convenience. However, it is easy to show that a meridional body force (e.g., created from tidal filtering) has an analogous and similar mean and gravity wave response as a zonal body force if the following substitutions are made: $\tilde{u} \rightarrow \tilde{v}$, $\tilde{v} \rightarrow \tilde{u}$, $\tilde{F}_x \rightarrow \tilde{F}_y$, $k \rightarrow l$, $l \rightarrow k$, $m \rightarrow m$, $\mathcal{S} \rightarrow \mathcal{S}$, $\mathcal{C} \rightarrow -\mathcal{C}$. For example, the secondary wave momentum fluxes from a meridional body force are

$$\overline{\tilde{u}_{\text{GW}} \tilde{w}_{\text{GW}}^*} = -\xi\zeta mk\omega^2[l^2(N^2 - \omega^2) + m^2f^2], \quad (5.21)$$

$$\overline{\tilde{v}_{\text{GW}} \tilde{w}_{\text{GW}}^*} = -\xi\zeta ml\omega^2[l^2(N^2 - \omega^2) + m^2f^2] \quad (5.22)$$

[substituting $\tilde{F}_x \rightarrow \tilde{F}_y$ in the expression for ζ in Eq. (5.7)], analogous to Eqs. (5.5) and (5.4), respectively. Rotation is unimportant for the secondary wave spectrum when

$$\sigma_y/\sigma_z \ll \sqrt{1 - \omega_c^2/N^2} N/f, \quad (5.23)$$

analogous to Eq. (5.8) (e.g., $\sigma_y/\sigma_z \ll 200$ at mid latitudes when $\omega_c \lesssim N/2$). And, the fraction of energy in secondary waves for a 3D, meridional body force is $E_{\text{GW}}/(\overline{E} + E_{\text{GW}}) \simeq \xi l_c^2/(\xi l_c^2 + k_c^2)$ when $\omega_c \ll N$ and when Eq. (5.23) is satisfied, analogous to Eq. (5.20). Thus, the responses to meridional body forces are easily understood. For example, a meridional body force with the same temporal and spatial scales as in Fig. 9 would create secondary waves carrying the same total upward momentum flux as in Fig. 9. Generalizing for any deep, 3D horizontal, localized body force, if the extent parallel to the force direction is equal to or less than the perpendicular extent, the energy in the secondary wave response is at least $100\xi/(\xi + 1)\%$ of the total energy, and the secondary wave momentum fluxes can be large for large forcing strengths. Most of these waves tend to propagate in the direction of the force (see Figs. 10 and 16a).

g. Secondary waves as a source of ducted waves

In the presence of a background wind, \overline{U} , the 2D dispersion relation is

$$m^2 = \frac{N^2}{(c_x - \overline{U})^2} - k^2. \quad (5.24)$$

If a secondary wave is created in a region such that $m^2 < 0$ at some altitude above and below z_0 , then this wave will be trapped or ducted. The turning level occurs when $m^2 = 0$, or for secondary waves with horizontal wavelength of $\lambda_x = 2\pi(c_x - \bar{U})/N$. Because the secondary wave spectrum created from a Gaussian body force is quite broad with a large range of horizontal and vertical scales (see Fig. 11), it is possible that body forces created from wave breaking in the mesosphere may be an efficient source of ducted secondary waves near the mesopause (as well as an efficient source of secondary waves with large enough phase speeds to avoid the duct and propagate into the thermosphere).

6. Summary and discussion

We have used a linear formulation of the atmospheric response to body forcing to examine the dependence of secondary gravity wave radiation on the spatial and temporal scales of a body force. The formulation was employed previously by Vadas and Fritts (2001a) to examine the partitioning of the body force influences among the mean response and secondary wave radiation. The mean response was found to have no dependence on the temporal character of the body force, whereas the gravity wave response is highly dependent on the spatial character and duration of the body force. This paper has explored these secondary wave responses more fully, anticipating their possibly important, but previously unappreciated, role in atmospheric dynamics at greater altitudes.

The first application of this formulation was to the 2D wave breaking arising from the growth with altitude of gravity waves generated by convection in the numerical simulation described by Holton and Alexander (2000). Here, the low-frequency response anticipated due to localized body forcing appears to account for the horizontal structure and slow temporal evolution of the horizontal wind field in the 2D simulation. In addition, our formulation generated high-frequency secondary waves, although with larger horizontal wavelength characteristics than were observed in the 2D simulation.

3D body forces, of course, are more representative of gravity wave dissipation in the atmosphere, and are the primary focus of this paper. Our hypothesis is that the zonal mean body force required to close the mesospheric jets, in fact, is applied sporadically in time, is composed of a large number of local body forces occurring on many spatial and temporal scales, and is thus a significant source of secondary gravity waves. These secondary waves are both neglected in large-scale modeling studies (because such models neither describe variable, small-scale wave dissipation nor resolve the waves arising from such forcing) and may account for substantial forcing of the atmosphere at even greater altitudes.

The results of our assessment of the gravity wave responses to 3D body forces may be summarized as follows:

- Secondary waves are radiated symmetrically (upward and downward; forward, backward, and laterally) along the direction of the body force and depending on the horizontal extent of (along and normal to) the body force;
- The character of secondary wave radiation depends on the spatial and temporal attributes of the body force, but not on its orientation and latitude;
- Secondary wave intrinsic frequencies depend both on the horizontal-to-vertical aspect ratio and on the temporal extent of the body force. Body forces that are deep, horizontally-

localized, and of short duration result in secondary waves having the highest intrinsic frequencies and momentum fluxes; and

- Secondary wave momentum fluxes vary quadratically with the body force strength.

If this view of gravity wave forcing of the middle atmosphere is appropriate, then the spatial and temporal variability accompanying the dissipation of localized gravity waves will lead to the sporadic generation of secondary waves having large vertical scales, and achieving large amplitudes and momentum fluxes as they propagate vertically. These waves will respond to varying wind shears at greater altitudes, and will thus impose variable momentum fluxes and flux divergences well into the thermosphere. The more sporadic and localized such wave dissipation (and generation) is, the larger the potential for increased variability and forcing at greater altitudes. It is not possible to quantify these effects at this time, but efforts are under way to assess the responses to specific forcing events and illustrate the potential variability.

Acknowledgments. S.L.Vadas and D.C. Fritts were supported by NASA contracts S-46331-G, S-46579-G, S-48971-G, and NAG5-02036, AFOSR contract F49620-98-C-0029, and NSF grants ATM-9618004 and ATM-9708633. M.J. Alexander was supported by NSF grant ATM-9907501. We thank our reviewers for their helpful comments.

APPENDIX A

Validity of the Linear Theory

In Appendix A of VF, we crudely estimated the validity of the linear theory using the analytic spectral solutions, and found that $u_0 < N\sigma_z$ in order that secondary wave-secondary wave interactions be small for impulsive forcings with $l_c = f = 0$. (Here, $N\sigma_z \simeq 30\text{ms}^{-1}$ when $\sigma_z = 1.5$ km.) We noted in VF that this was an underestimate even for impulsive forcings, and that the solutions to slower forcings would still be linear at much larger forcing strengths. However, it was beyond the scope of that paper to calculate more carefully where the linear theory breaks down. In Fig. 20, we show the forcing strengths for 2D body forces 7km deep whereby the zonal momentum wave-wave interactions equal the largest of 1) the zonal accelerations, or 2) the zonal pressure gradients. Here, the zonal wave-wave interaction is $u\partial u/\partial x + w\partial u/\partial z$, the zonal acceleration is $\partial u/\partial t$, and the zonal pressure gradient is $(\partial p'/\partial x)/\bar{\rho}$. All linear and nonlinear terms are calculated using the linear solutions after inverting Eqs. (3.13)-(3.17) of VF to physical space. Although nearly impulsive, very short horizontal wavelength forcings do require somewhat smaller force strengths, in general the linear theory is valid for forcing strengths of order or greater than the speed of sound (which is $c_s \simeq 300\text{ms}^{-1}$). Slower forcings require less restrictive forcing strengths. Doubling the forcing depth enables the force strength to be doubled within the linear theory for the same horizontal to vertical aspect ratios. Therefore, nonlinear interactions are generally only important when compressible effects are also important. However, even though nonlinear effects are important during 3D wave breaking, the dynamical effects of compressibility have been found to be unimportant even for primary waves with very high intrinsic frequencies (Fritts et al., 1994).

REFERENCES

- Andreassen, Ø., C.E. Wasberg, D.C. Fritts and J.R. Isler, 1994: Gravity wave breaking in two and three dimensions. 1. Model description and comparison of two-dimensional evolutions, *J. Geophys. Res.*, **99**, 8095–8108.
- Andreassen, Ø., P.Ø. Hvidsten, D.C. Fritts and S. Arendt, 1998: Vorticity dynamics in a breaking internal gravity wave. Part 1. Initial instability evolution, *J. Fluid Mech.*, **367**, 27–46.
- Andrews, D. G., J. R. Holton, and C. B. Leovy, 1987: Middle atmosphere dynamics, Academic Press, Florida.
- Bacmeister, J.T. and M.R. Schoeberl, 1989: Breakdown of vertically propagating two-dimensional gravity waves forced by orography, *J. Atmos. Sci.*, **46**, 2109–2134.
- Beagley, S.R., J. de Grandpré, J.N. Koshyk, N.A. McFarlane and T.G. Shepherd, 1997: Radiative-dynamical climatology of the first-generation Canadian middle atmosphere model, *Atmos. Ocean.*, **35**, 293–331.
- Bühler, O., M. E. McIntyre, and J. F. Scinocca, 1999: On shear-generated gravity waves that reach the mesosphere. Part I: wave generation, *J. Atmos. Sci.*, **56**, 3749–3763.
- Chimonas, G., and J. R. Grant, 1984: Shear excitation of gravity waves. Part II: Upscale scattering from Kelvin-Helmholtz waves, *J. Atmos. Sci.*, **41**, 2278–2288.
- Dunkerton, T. J., 1987: Effect of nonlinear instability on gravity wave momentum transport, *J. Atmos. Sci.*, **44**, 3188–3209.
- Fovell, R. D. Durran, and J. R. Holton, 1992: Numerical simulations of convectively generated stratospheric gravity waves, *J. Atmos. Sci.*, **49**, 1427–1442.
- Franke, P.M., 1996: Nonlinear behavior in the propagation of atmospheric gravity waves, PhD Thesis in Electrical Engineering, University of Illinois at Urbana-Champaign.
- Franke, P.M. and W.A. Robinson, 1999: Nonlinear behavior in the propagation of atmospheric gravity waves, *J. Atmos. Sci.*, **56**, 3010–3027.
- Fritts, D. C., and R. A. Vincent, 1987: Mesospheric momentum flux studies at Adelaide, Australia: Observations and a gravity wave/tidal interaction model, *J. Atmos. Sci.*, **44**, 605–619.
- Fritts, D. C., 1984: Shear excitation of atmospheric gravity waves. Part II: Nonlinear radiation from a free shear layer, *J. Atmos. Sci.*, **41**, 524–537.
- Fritts, D. C., and L. Yuan, 1989: Measurement of momentum fluxes near the summer mesopause at Poker Flat, Alaska, *J. Atmos. Sci.*, **46**, 2569–2579.
- Fritts, D. C., and Z. Luo, 1992: Gravity wave excitation by geostrophic adjustment of the jet stream, Part 1: Two-dimensional forcing, *J. Atmos. Sci.*, **49**, 681–697.
- Fritts, D. C., L. Yuan, M.H. Hitchman, L. Coy, E. Kudeki, and R.F. Woodman, 1992: Dynamics of the equatorial mesosphere observed using the Jicamarca MST radar during June and August 1987, *J. Atmos. Sci.*, **49**, 2353–2371.
- Fritts, D.C., J.R. Isler, and Ø. Andreassen, 1994: Gravity wave breaking in two and three dimensions. 2. Three-dimensional evolution and instability structure, *J. Geophys. Res.*, **99**, 8109–8123.
- Fritts, D.C., S. Arendt, and Ø. Andreassen, 1998: Vorticity dynamics in a breaking internal gravity wave. Part 2. Vortex interactions and transition to turbulence, *J. Fluid Mech.*, **367**, 47–65.

- Fritts, D.C., S.L. Vadas, and Y. Yamada, 2002: An estimate of strong local body forcing and gravity wave radiation based on OH airglow and meteor radar observations, *Geophys. Res. Lett.*, **xx**, in press.
- Garcia, R.R. and S. Solomon, 1985: The effect of breaking gravity waves on the dynamics and chemical composition of the mesosphere and lower thermosphere, *J. Geophys. Res.*, **90**, 3850–3868.
- Hamilton, K., R.J. Wilson, J.D. Mahlman and L.J. Umscheid, 1995: Climatology of the SKYHI troposphere-stratosphere-mesosphere general circulation model, *J. Atmos. Sci.*, **52**, 5–43.
- Holton, J. R., 1983: The influence of gravity wave breaking on the general circulation of the middle atmosphere, *J. Atmos. Sci.*, **40**, 2497–2507.
- Holton, J. R. and M. J. Alexander, 1999a: Gravity waves in the mesosphere generated by tropospheric convection, *Tellus*, **51A-B**, 45–58.
- Huang, C.M., F.S. Kuo, H.Y. Lue, and C.H. Liu, 1992: Numerical simulations of the saturated gravity wave spectra in the atmosphere, *J. Atmos. Terres. Phys.*, **54**, 129–142.
- Huang, T.Y.W. and A.K. Smith, 1995: Dynamical and chemical feedback in a two-dimensional interactive model of the middle atmosphere, *J. Geophys. Res.*, **100**, 11085–11104.
- Klostermeyer, J., 1991: Two- and three-dimensional parametric instabilities in finite amplitude internal gravity waves, *Geophys. Astrophys. Fluid Dyn.*, **64**, 1–25.
- LeLong, M.-P. and T.J. Dunkerton, 1998: Inertia-gravity wave breaking in three dimensions. Part I: Convectively stable waves, *J. Atmos. Sci.*, **55**, 2473–2488.
- Liu, H.-L., P.B. Hays, and R.G. Roble, 1999: A numerical study of gravity wave breaking and impacts on turbulence and mean state, *J. Atmos. Sci.*, **56**, 2152–2177.
- Luo, Z., and D. C. Fritts, 1993: Gravity wave excitation by geostrophic adjustment of the jet stream, Part II: Three-dimensional forcing, *J. Atmos. Sci.*, **50**, 104–115.
- McComas, C. H., and F. P. Bretherton, 1977: Resonant interaction of oceanic internal waves, *J. Geophys. Res.*, **82**, 1397–1412.
- McLandress, C., 1998: On the importance of gravity waves in the middle atmosphere and their parameterization in general circulation models, *J. Atmos. Solar Terres. Phys.*, **60**, 1357–1383.
- Pfister, L., K. R. Chan, T. P. Bui, S. Bowen, M. Legg, B. Gary, K. Kelly, M. Proffitt, and W. Starr, 1993: Gravity waves generated by a tropical cyclone during the STEP tropical field program: A case study, *J. Geophys. Res.*, **98**, 8611–8638.
- Prusa, J.M., P.K. Smolarkiewicz, R.R. Garcia, 1996: Propagation and breaking at high altitudes of gravity waves excited by tropospheric forcing, *J. Atmos. Sci.*, **53**, 2186–2216.
- Reid, I.M. and R.A. Vincent, 1987: Measurements of mesospheric gravity wave momentum fluxes and mean flow accelerations at Adelaide, Australia, *J. Atmos. Terres. Phys.*, **49**, 443–460.
- Reid, I.M., R. Ruster, P. Czechowsky, and G. Schmidt, 1988: VHF radar measurements of momentum flux in the summer polar mesosphere over the Andenes (69°N, 16°E), Norway, *Geophys. Res. Lett.*, **15**, 1263–1266.
- Rind, D., R. Suozzo, and N. K. Balachandran, A. Lacis, and G. Russell, 1988: The GISS global climate-middle atmosphere model. Part I: Model structure and climatology, *J. Atmos. Sci.*, **45**, 329–370.

- Roble, R.G. and E.C. Ridley, 1994: A thermosphere-ionosphere-mesosphere-electrodynamics general circulation model (TIME-GCM): equinox solar cycle minimum simulations (30-500km), *Geophys. Res. Lett.*, **21**, 417–420.
- Satomura, T. and K. Sato, 1999: Secondary generation of gravity waves associated with the breaking of mountain waves, *J. Atmos. Sci.*, **56**, 3847–3858.
- Scinocca, J. F., and R. Ford, 2000: The nonlinear forcing of large-scale internal gravity waves by stratified shear instability, *J. Atmos. Sci.*, **57**, 653–672.
- Tsuda, T., Y. Murayama, M. Yamamoto, S. Kato, and S. Fukao, 1990: Seasonal variation of momentum flux in the mesosphere observed with the MU radar, *Geophys. Res. Lett.*, **17**, 725–728.
- Vadas, S. L., and D. C. Fritts, 2001a: Gravity wave radiation and mean responses to local body forces in the atmosphere, *J. Atmos. Sci.*, **58**, 2249–2279.
- Vadas, S. L. and D. C. Fritts, 2001b: “Mechanism for the generation of secondary waves in wave breaking regions”, 13th Conference on Atmospheric and Oceanic Fluid Dynamics in Breckenridge, Colorado, June, 2001.
- Vadas, S. L., and D. C. Fritts, 2002: The importance of spatial variability in the generation of secondary gravity waves from local body forces, *Geophys. Res. Lett.*, **xx**, in press.
- Vanneste, J., 1995: The instability of internal gravity waves to localized disturbances, *Ann. Geophys.*, **13**, 196–210.
- Walterscheid, R.L. and G. Schubert, 1990: Nonlinear evolution of an upward propagating gravity wave: overturning, convection, transience and turbulence, *J. Atmos. Sci.*, **47**, 101–125.
- Yamada, Y., H. Fukunishi, T. Nakamura, and T. Tsuda, 2001: Breaking of small-scale gravity wave and transition to turbulence observed in OH airglow, *Geophys. Res. Lett.*, **28**, 2153–2156.
- Yeh, K. C., and C. H. Liu, 1981: The instability of atmospheric gravity waves through wave-wave interactions, *J. Geophys. Res.*, **86**, 9722–9728.
- Zhu, X., and J. R. Holton, 1987: Mean fields induced by local gravity-wave forcing in the middle atmosphere, *J. Atmos. Sci.*, **44**, 620-630.

FIGURE CAPTIONS

Fig. 1: Contours of the zonal wind perturbation with respect to the storm frame at $t = 4$ hrs in ms^{-1} from the simulation illustrated in HA (personal communication, J. R. Holton). (Zonal wind perturbation contours were not shown in HA.)

Fig. 2: Reprinted from Fig. 8 of Holton and Alexander (1999), with permission from Tellus.

Fig. 3: Response to the case I body force. a-b): $t = 11$ min and c-d): $t = 30$ min. The left-hand column shows the zonal velocity contours, while the right-hand column shows the vertical velocity contours. Each plot is scaled by its maximum value, u_{max} or w_{max} . The solid contours indicate values from 0.1 to 1.0 with 0.1 increments, and the dashed contours indicate the values from -0.1 to -1.0 with -0.1 increments. For the vertical velocity contours, only the 0.5 and -0.5 contours are shown as light and dark shaded contours, respectively. The dot lines in each downward-eastward quadrant show the paths gravity waves with $\omega = \omega_c$ would travel from the body force center. The hatched regions indicate where the body force is greater than 10% of its maximum value. The maximum amplitudes are $u_{\text{max}} = 46$ and 14 ms^{-1} and $w_{\text{max}} = 3.1$ and 1.9 ms^{-1} at $t = 11$ and 30 min, respectively. Here, $\sigma_t = \tau_c$, $N_x = 1024$ and $N_z = 2048$.

Fig. 4: Post-forcing vertical wind power spectral density for case I body forces. Shown with solid and dash lines are $\sigma_t = \tau_c$ and $\sigma_t = 2\tau_c$, respectively. The dot lines show the locations of ω_c , $9\sigma_x$, $9\sigma_z$, and $\omega_c(9\sigma_x/2\pi)$ in (a)-(d), respectively. Here, $9\sigma_x$ and $9\sigma_z$ are twice the width and depth of the body force, respectively. Here $t = 2\sigma_t$, $N_x = 1024$, and $N_z = 2048$. Note that the peak shapes and maximal wavenumbers do not depend on the force strength u_0 .

Fig. 5: Same as in Fig. 4, except for case II forces.

Fig. 6: (a): Case II force tilted eastward $\psi = 14$ degrees. This angle mimics the case II tilts in Fig. 1. (b): Secondary wave vertical velocity contours at $t = 30$ min scaled by $w_{\text{max}} = 1.6 \text{ ms}^{-1}$ from (a). The solid contours indicate values from 0.1 to 0.9 with 0.2 increments, and the dashed contours indicate the values from -0.1 to -0.9 with -0.2 increments. (c): momentum flux spectra in covariance content form from (a) at $t = \sigma_t$. The solid, dash and dash-dot show the total, eastward, and westward momentum fluxes, respectively. (d): Two case I, untilted forces aligned such that the horizontal and vertical separations between their centers are $4.5\sigma_x$ and $4.5\sigma_z$, respectively. (e): Vertical velocity contours at $t = 13$ min scaled by $w_{\text{max}} = 6.0 \text{ ms}^{-1}$ from (d). Contours are as in (b). (f): As in (c) but from (d). To generate these illustrations, $\sigma_t = \tau_c$, $N_x = 512$, and $N_z = 1024$.

Fig. 7: Zonal wind spectra in covariance content form evaluated at $t = 2\sigma_t$ for three case I body forces separated horizontally by differing distances but at the same altitude. The solid, dash, dash-dot, and dash-dot-dot-dot lines correspond to horizontal separation distances of 0, \mathcal{D}_x , $2\mathcal{D}_x$, and $3\mathcal{D}_x$, where $\mathcal{D}_x \equiv 4.5\sigma_x$. The amplitude of the 0 separation forcing is reduced by 3 in order to compensate for its increased spectral amplitude [since $(3u_0)^2 \neq 3u_0^2$]. To generate these illustrations, $\sigma_t = \tau_c$, $N_x = 512$, and $N_z = 1024$.

Fig. 8: The solid, dash, dash-dot, and dash-dot-dot-dot lines show the behavior of ξ for $\sigma_t = 0.1\tau_c$, $0.5\tau_c$, τ_c , and $2\tau_c$, respectively. The dotted line shows $\omega = \omega_c$. For this illustration, $\sigma_x = \sigma_y = 22.2$ km and $\sigma_z = 4.4$ km. Only the $\sigma_t \geq \tau_c$ cases are relevant for the body force mechanism as arising from gravity wave breaking.

Fig. 9: Response to a 3D zonal body force with $\sigma_x = \sigma_y = 22.2$ km and $\sigma_z = 4.4$ km. a-b): Post-forcing zonal mean wind, scaled by its maximum amplitude of $\bar{u} = 30$ ms⁻¹. c-d): zonal wind at $t = 25$ min, scaled by its maximum gravity wave amplitude of 2.5 ms⁻¹. e-f): zonal wind at $t = 50$ min, scaled by its maximum gravity wave amplitude of 1.0 ms⁻¹. The solid contours indicate values from 0.1 to 1.0 with 0.1 increments, and the dashed contours indicate the values from -0.1 to -1.0 with -0.1 increments. The lightly shaded region indicates where the body force is greater than 10% of its maximum value. For (c)-(f), the zonal wind contours larger than the maximum gravity wave amplitudes are not shown. For this illustration, $f = 0$, $\sigma_t = \tau_c$, $N_x = N_y = 128$, and $N_z = 256$.

Fig. 10: Momentum fluxes at $z - z_0 = 42$ km and $t = 25$ min from Fig. 9. The contour intervals are 0.01 m²s⁻². The light shading shows the location of waves with $\omega = \omega_c$.

Fig. 11: a): Total momentum flux for the secondary waves in a single quadrant (i.e., propagating upward and eastward, northward and southward) created from the body force in Fig. 9 with $f = 0$. Light solid contours are separated by 0.01 m²s⁻². Thick, short dash contours indicate $c_x \equiv \omega/k$ in 100m/s intervals when $l = 0$. Long dash contours indicate $c_{gz} \equiv \partial\omega/\partial m$ in 15m/s intervals. b): Light solid contours: same as in (a). Dash contours: $f = 10^{-4}$ s⁻¹ (mid latitudes). For both cases, the total momentum fluxes per quadrant are 3.1 m²s⁻². For this illustration, $\sigma_t = \tau_c$, $t = \sigma_t$, $N_x = N_y = 128$, and $N_z = 256$.

Fig. 12: Total momentum flux associated with the secondary waves in a single quadrant created from the body force in Fig. 9 for differing force durations. All contours are separated by 0.015 m²s⁻². The light solid lines are for $\sigma_t = 0.5\tau_c$, the dash lines are for $\sigma_t = \tau_c$, and the dark dash-dot lines are for $\sigma_t = 2\tau_c$. The evaluation times are $t = 2\sigma_t$ for $\sigma_t/\tau_c < 1$, and $t = \sigma_t$ otherwise. To generate this illustration, $f = 0$, $N_x = N_y = 128$ and $N_z = 256$.

Fig. 13: Attributes of the total momentum flux PSD in covariance content form for 3D body forces with $\sigma_z = 4.4$ km and $\sigma_x = \sigma_y$. (a): maximum frequency divided by ω_c , (b): maximum zonal wavelength, (c): maximum meridional wavelength, (d): maximum vertical wavelength. The diamonds and triangles show the peak values of the spectra for $\sigma_x = 11$ and 132 km, respectively, and the hatched regions show where the values of these spectra are greater than one-half the maximum value. The arrows show where $\omega/\omega_c = 1$, $\lambda_x = 9\sigma_x$, $\lambda_y = 9\sigma_y$, and $\lambda_z = 9\sigma_z$ in (a)-(d), respectively. Here, $9\sigma_x$, $9\sigma_y$, and $9\sigma_z$ are twice the widths and depth of the body force. To generate these illustrations, $f = 0$, $N_x = 128$ and $N_y = N_z = 256$. The evaluation times are $t = 2\sigma_t$ for $\sigma_t/\tau_c < 1$, and $t = \sigma_t$ otherwise. This figure does not depend on u_0 . Only the $\sigma_t \geq \tau_c$ cases are relevant for the body force mechanism as arising from gravity wave breaking, as indicated by the ‘‘GWB’’ labels.

Fig. 14: Upgoing momentum flux associated with the secondary waves created from the Fig. 9

body force but which is tilted by 14 degrees with respect to the vertical. a): Upward zonal momentum flux. b): Upward meridional momentum flux. Contour intervals are $0.01\text{m}^2\text{s}^{-2}$. The upward zonal momentum fluxes are $4.7\text{m}^2\text{s}^{-2}$ eastward and $0.6\text{m}^2\text{s}^{-2}$ westward, while the upward meridional momentum fluxes are $1.0\text{m}^2\text{s}^{-2}$ northward and $1.0\text{m}^2\text{s}^{-2}$ southward. For this illustration, $\sigma_t = \tau_c$, $t = \sigma_t$, $f = 0$, $N_x = N_y = 128$, and $N_z = 256$.

Fig. 15: Momentum flux PSD in covariance content form in m^2s^{-2} for 2D and 3D body forces with $\sigma_z = 4.4$ km. Solid lines are for a 2D latitudinally-symmetric body force with $\sigma_x = 22.2$ km at mid latitudes. Dash and dash-dot lines are for a 2D zonally-symmetric body force with $\sigma_y = 22.2$ km at mid and high latitudes, respectively. Dash-dot-dot-dot lines are for a 3D body force with $\sigma_x = \sigma_y = 22.2$ km at mid latitudes. Mid latitude forces occur at 45 degrees, while the high-latitude body force occurs at 70 degrees. Here, $\sigma_t = \tau_c$ and $t = 2\sigma_t$. In addition, $N_x = 256$ and $N_z = 512$ for the latitudinally-symmetric force, $N_y = 256$ and $N_z = 512$ for the zonally-symmetric forces, and $N_x = N_y = 128$ and $N_z = 256$ for the 3D force. Note that the locations of the maxima (i.e., ω or m) do not depend on u_0 .

Fig. 16: a): α_{uw} and β_{vw} are shown as solid and dash lines, respectively. The vertical dotted line shows where where $\bar{E} = E_{\text{GW}}/\xi$. b): The estimated fraction of energy in gravity waves, $E_{\text{GW}}/(\bar{E} + E_{\text{GW}})$, is shown as a solid line. The estimated fraction of energy in the mean response, $\bar{E}/(\bar{E} + E_{\text{GW}})$, is shown as a dash line. Here, $\sigma_t = \tau_c$ and $\omega \simeq \omega_c$ so that $\xi = 1/4$. The quantity $\sqrt{\alpha_{uw}^2 + \beta_{vw}^2}$ is shown as triangles.

Fig. 17: a): Shaded contour of a body force with $\sigma_x = 22.2$ km, $\sigma_y = 222$ km, and $\sigma_z = 4.4$ km. The light and dark shaded regions indicates where the body force is greater than 10% and 50% of its maximum value, respectively. b): Total secondary wave momentum flux in m^2s^{-2} per quadrant from (a). c): Shaded contour of the force with $\sigma_x = 222$ km, $\sigma_y = 22.2$ km, $\sigma_z = 4.4$ km. d): Total secondary wave momentum flux in m^2s^{-2} per quadrant from (c). For these illustrations, $f = 10^{-4}$ rad/s, $\sigma_t = \tau_c$, and $t = 2\sigma_t$. For (a)-(b), $N_x = N_y = 128$, and $N_z = 512$. For (c)-(d), $N_x = 32$, $N_y = 256$, and $N_z = 1024$.

Fig. 18: Zonal wind spectra in covariance content form evaluated at $t = \sigma_t$ for three 3D body forces equally separated in the zonal direction. Each body force has $\sigma_x = 22.2$ km and $\sigma_z = 4.4$ km. (a): $\sigma_y = \sigma_x$. (b): $\sigma_y = 10\sigma_x$. The solid, dash, dash-dot, and dash-dot-dot-dot lines correspond to zonal separation distances of 0, \mathcal{D}_x , $2\mathcal{D}_x$, and $3\mathcal{D}_x$, where $\mathcal{D}_x \equiv 4.5\sigma_x$. The amplitude of the 0 separation forcing is reduced by 3 in order to compensate for its increased spectral amplitude [since $(3u_0)^2 \neq 3u_0^2$]. To generate these illustrations, $f = 0$, $\sigma_t = \tau_c$, $N_x = N_y = 128$, and $N_z = 256$. All body forces are centered at $y = y_0$ and $z = z_0$.

Fig. 19: (a): Horizontal slice of 16 3D body forces centered at $z = z_0$ and which are equally-spaced in x and y by $2\mathcal{D}_x$. Each body force is the same as in Fig. 9. Contours are spaced by $0.2u_0$. (b): The body force distributions at $y - y_0 = 100\text{km}$ and $z = z_0$. The solid line shows the distribution in (a). The dash, dash-dot, and dash-dot-dot-dot lines show the distribution in (a) but horizontally averaged over 50, 100, and 150 km wide regions, respectively. (c): The secondary wave momentum flux spectra in covariance content form using the same linetypes as in (b). For this illustration, $f = 0$, $\sigma_t = \tau_c$, $t = \sigma_t$, $N_x = 128$, and $N_y = N_z = 256$.

Fig. 20: Force strengths, u_0 (in ms^{-1}), such that the nonlinear wave-wave interactions in the zonal momentum equation equal the largest of 1) the zonal acceleration or 2) the zonal pressure gradient. The nonlinear and pressure gradient terms are calculated at $t = \sigma_t$, and the zonal accelerations are the changes in the zonal winds between $t = \sigma_t$ and $t = 1.01 \sigma_t$. All terms are calculated after inverting the linear solutions to (x, z) space. The absolute value of each term is averaged over each horizontal slice, and then the smallest force amplitude in height is shown. All forces are 2D zonal forces with $\sigma_z = 1.5$ km, $f = 0$, and $N_x = N_z = 1024$.

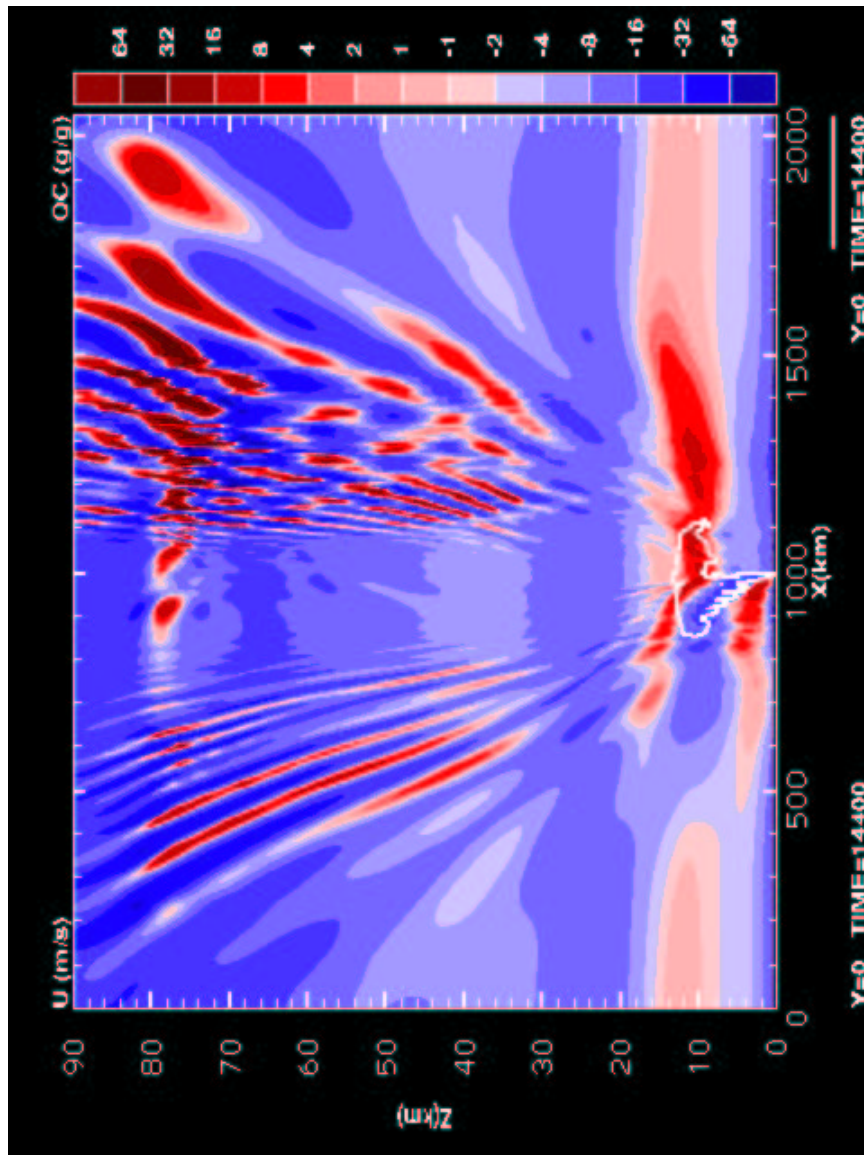


Figure 1:

Figure 2:

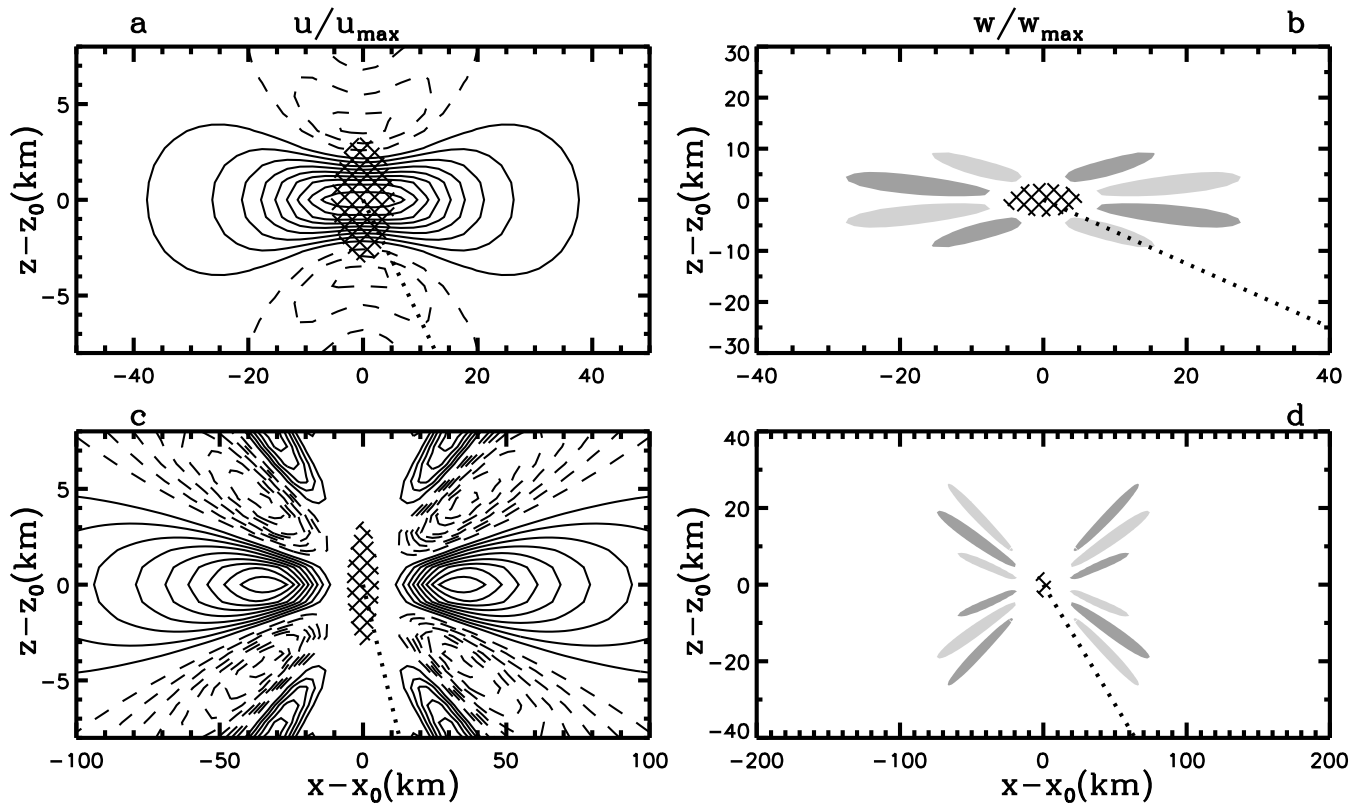


Figure 3:

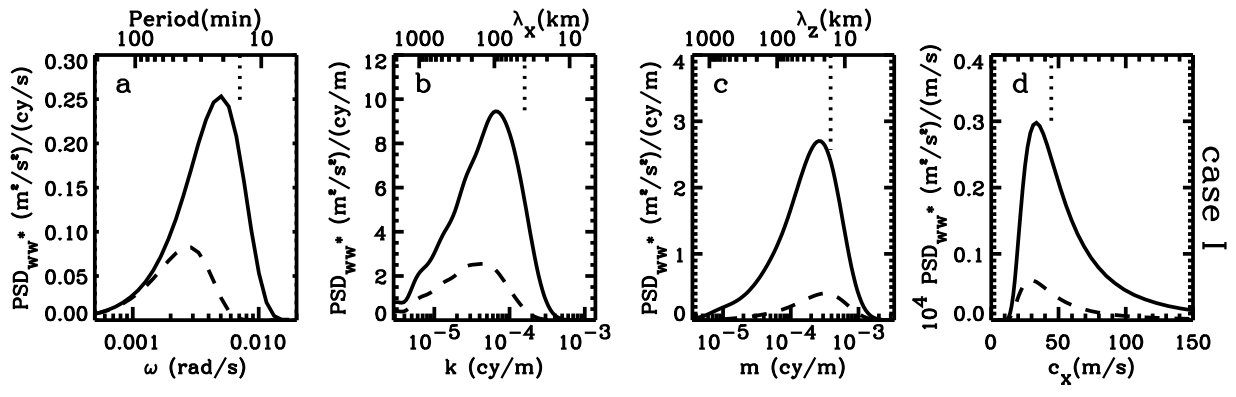


Figure 4:

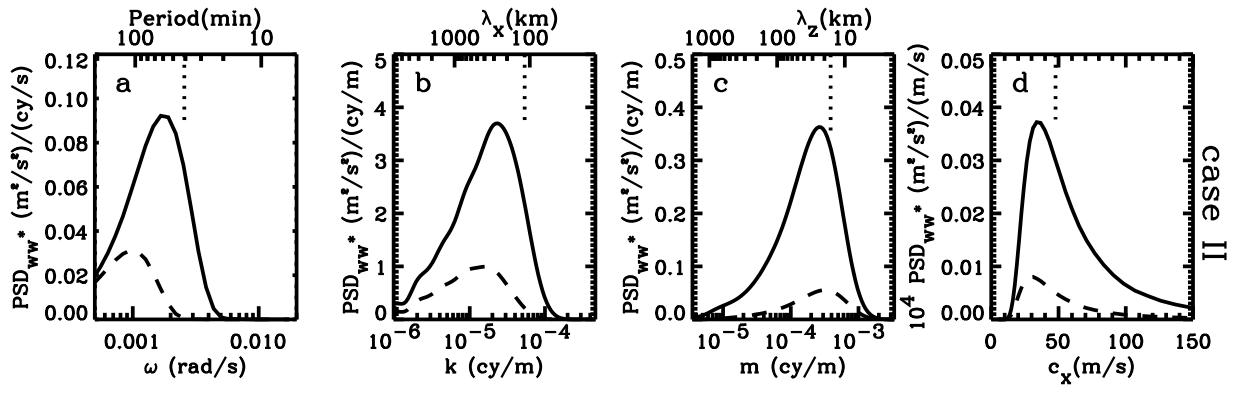


Figure 5:

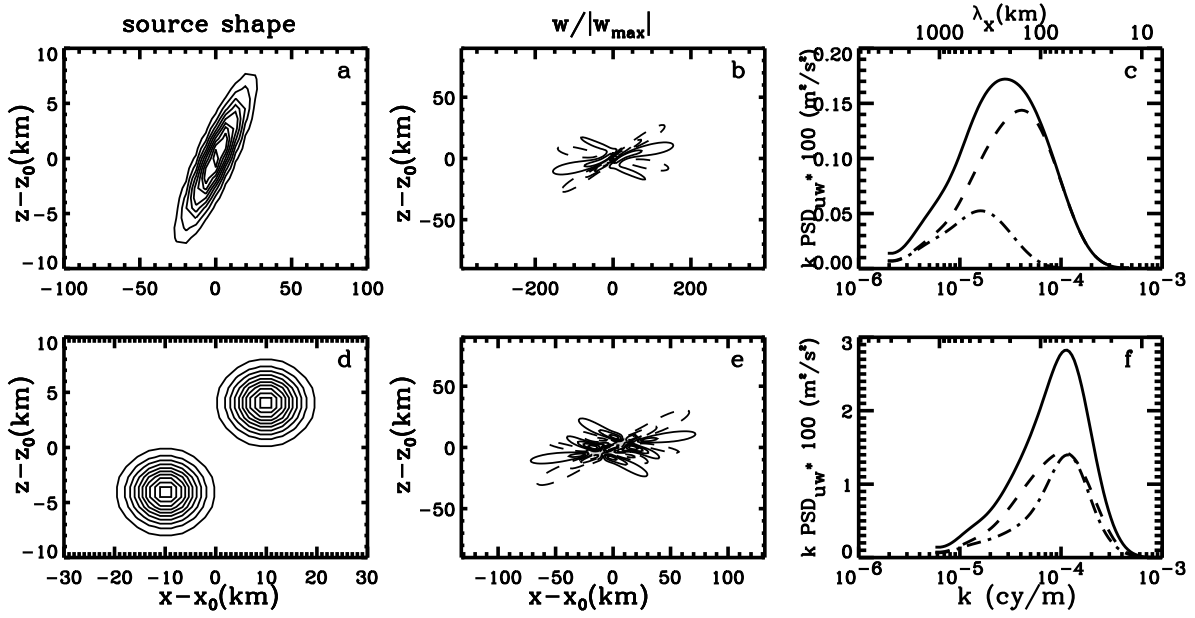


Figure 6:

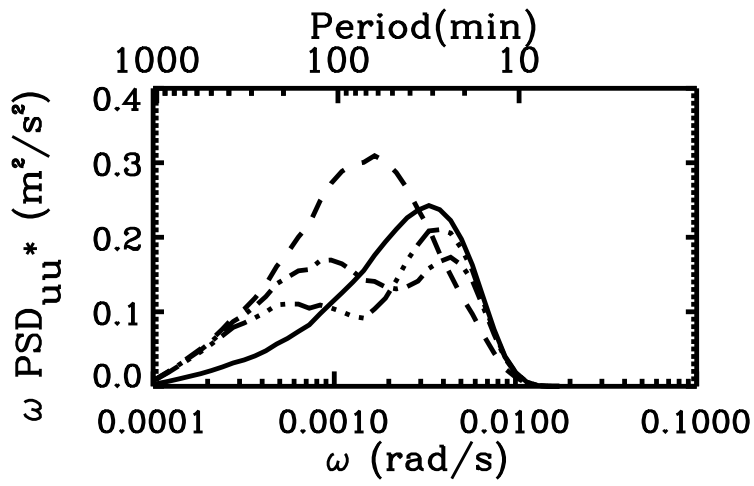


Figure 7:

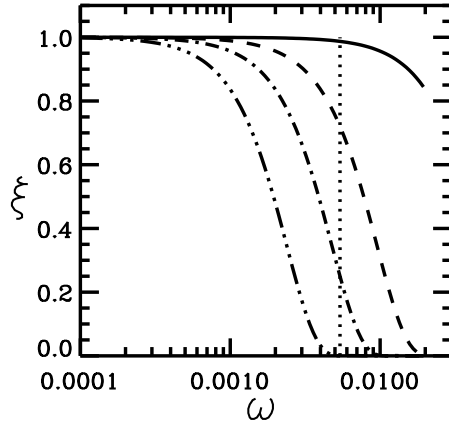


Figure 8:

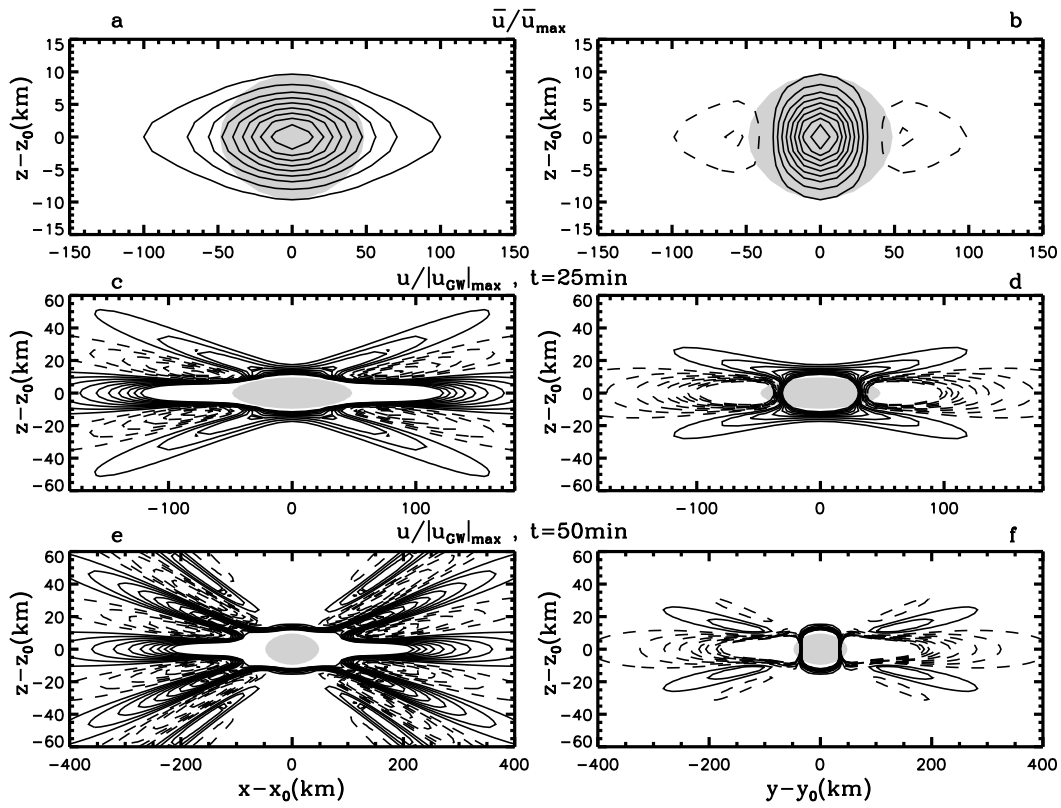


Figure 9:

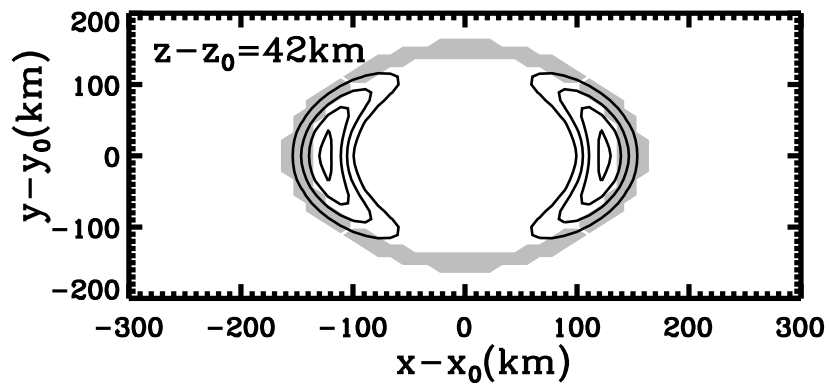


Figure 10:

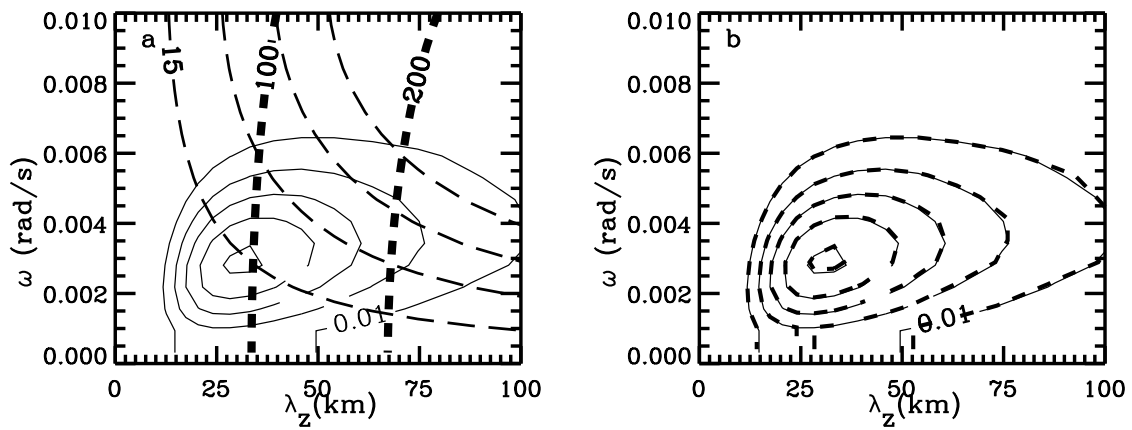


Figure 11:

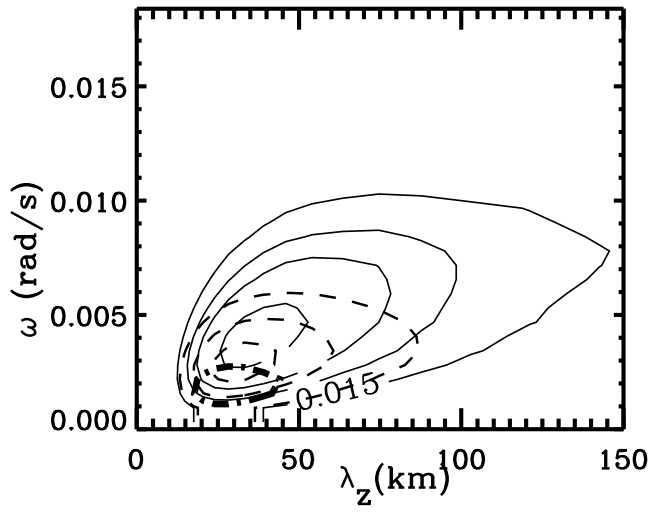


Figure 12:

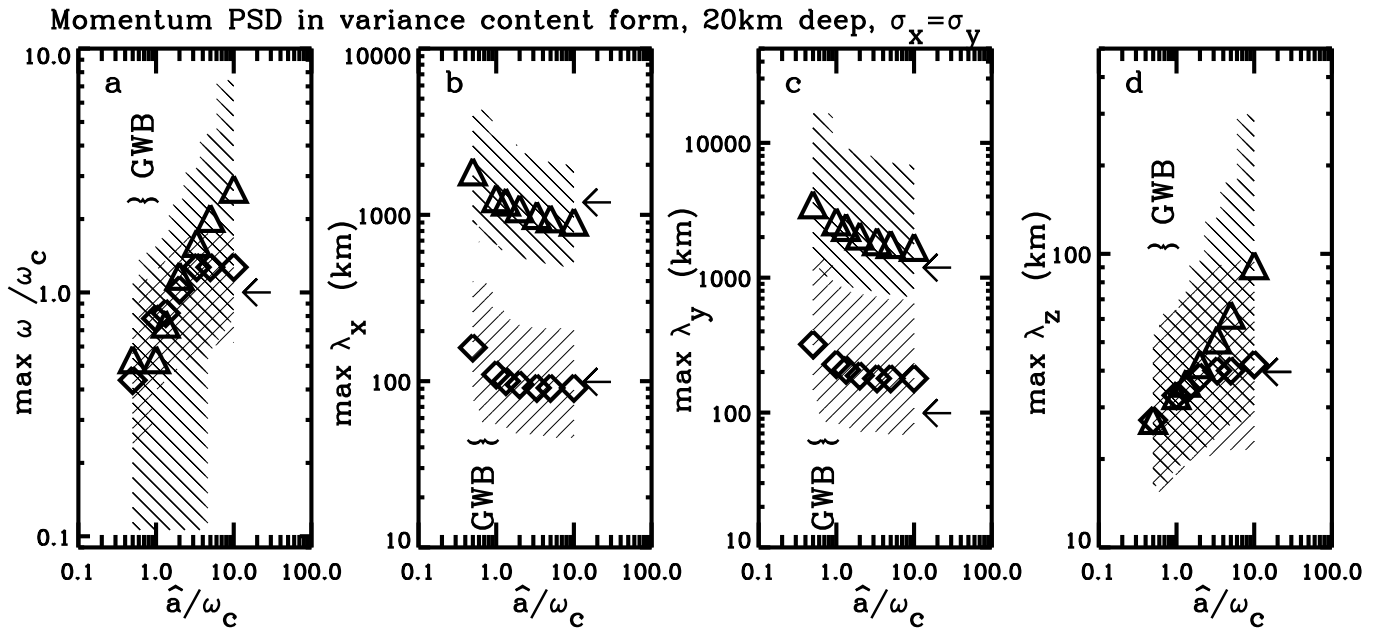


Figure 13:

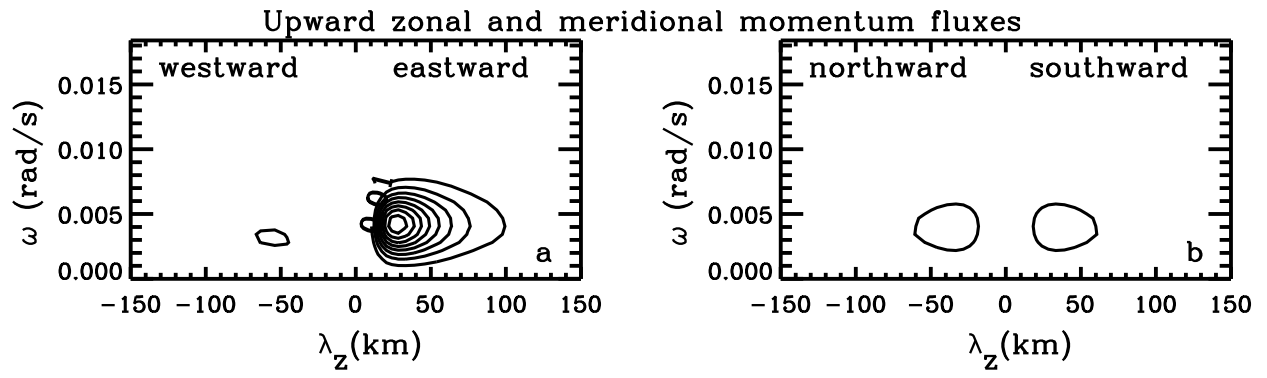


Figure 14:

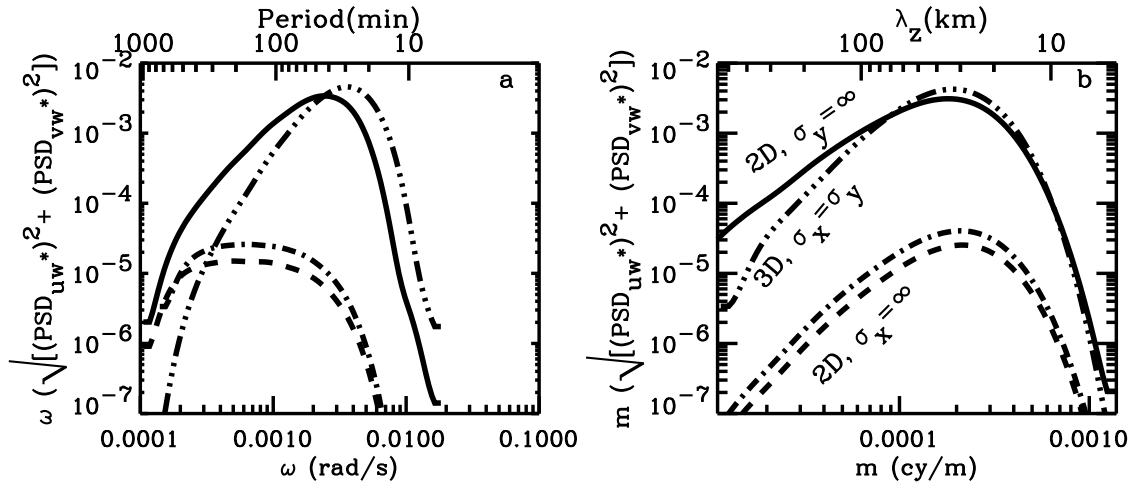


Figure 15:

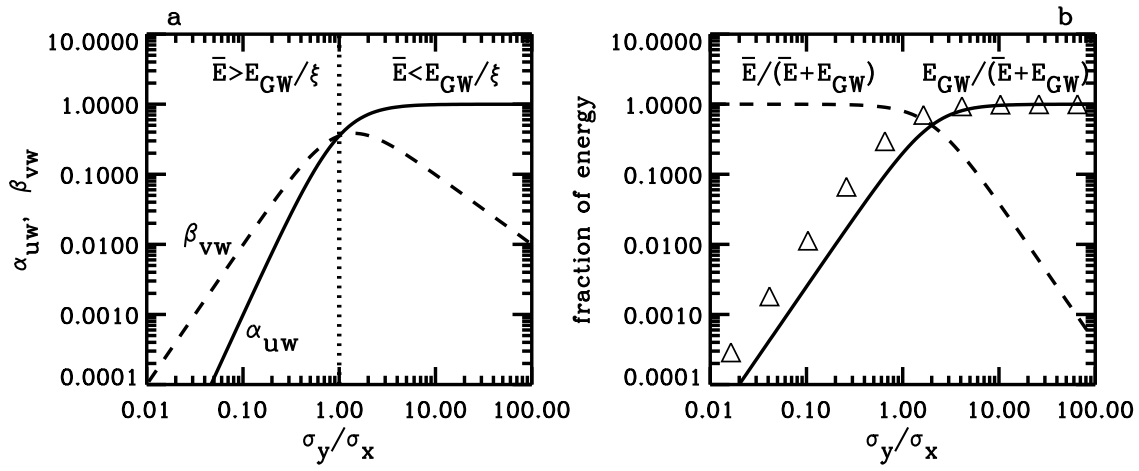


Figure 16:

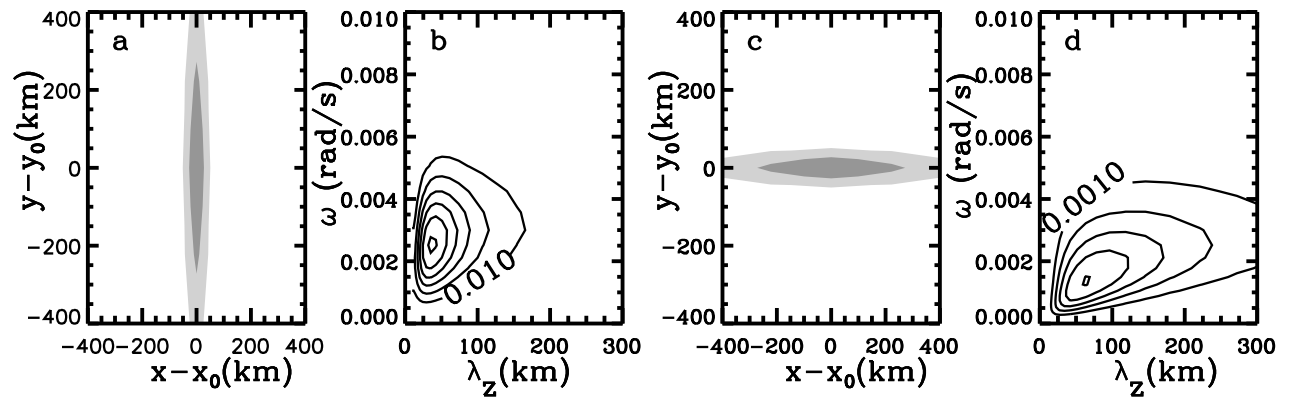


Figure 17:

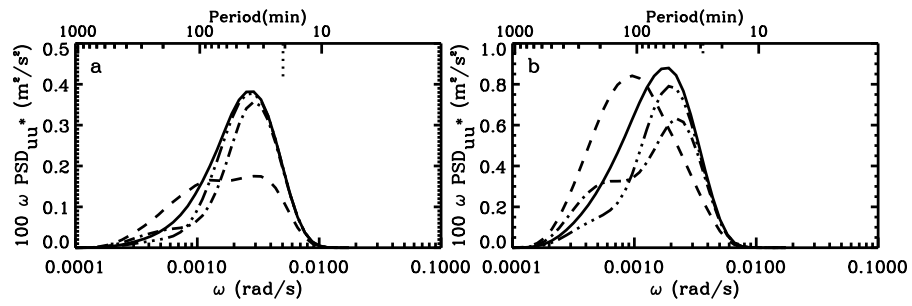


Figure 18:

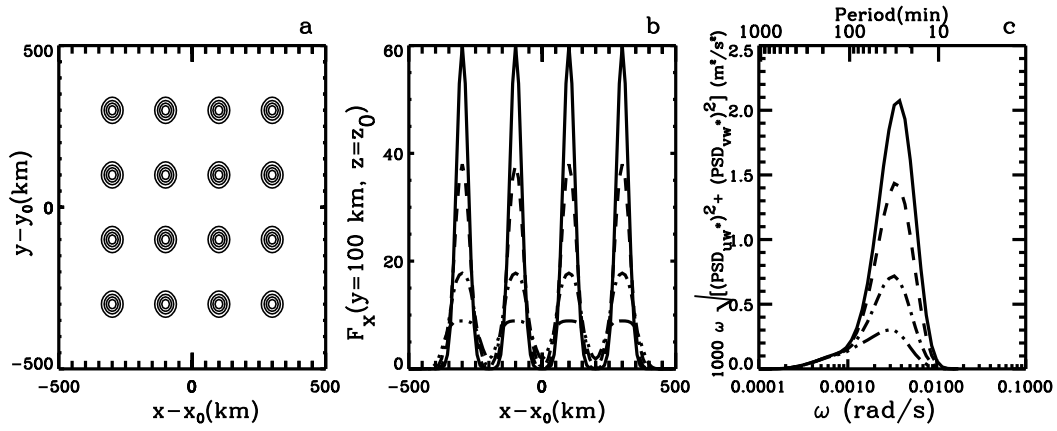


Figure 19:

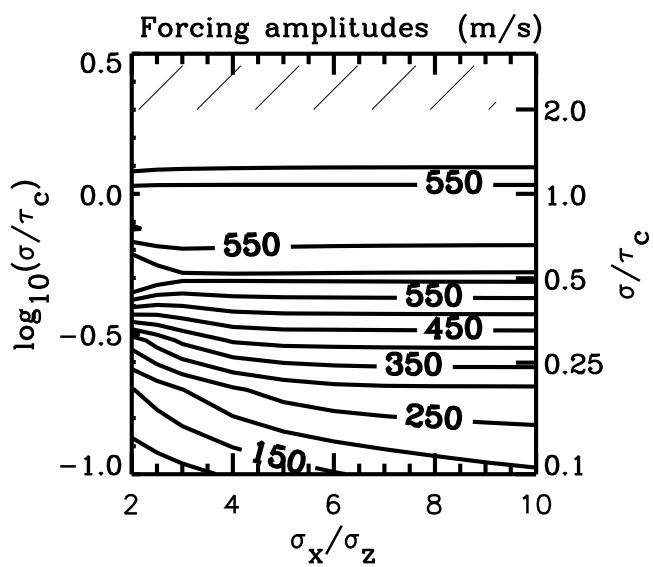


Figure 20: